Human Molecular Genetics, 2017, Vol. 26, No. 18 3466–3481

doi: 10.1093/hmg/ddx227
Advance Access Publication Date: 19 June 2017
Original Article

ORIGINAL ARTICLE

Loss of native α-synuclein multimerization by strategically mutating its amphipathic helix causes abnormal vesicle interactions in neuronal cells

Ulf Dettmer[1,*], Nagendran Ramalingam[2], Victoria E. von Saucken[1], Tae-Eun Kim[1], Andrew J. Newman[1], Elizabeth Terry-Kantor[1], Silke Nuber[1], Maria Ericsson[3], Saranna Fanning[4], Tim Bartels[1], Susan Lindquist[4,5,†], Oren A. Levy[2] and Dennis Selkoe[1]

[1]Ann Romney Center for Neurologic Diseases, Department of Neurology, Brigham and Women's Hospital and Harvard Medical School, Boston, MA 02115, USA, [2]Department of Neurology, Columbia University Medical Center, New York, NY 10032, USA, [3]Department of Cell Biology, Harvard Medical School, Boston, MA 02115, USA, [4]Whitehead Institute for Biomedical Research, Cambridge, MA 02142, USA and [5]HHMI, Department of Biology, MIT, Cambridge, MA 02139, USA

*To whom correspondence should be addressed at: Ann Romney Center for Neurologic Diseases, Department of Neurology, Brigham and Women's Hospital, The Brigham Building for Transformative Medicine, Room 10002-M, 60 Fenwood Road, Boston, MA 02115, USA. Tel: +16175255761; Fax: +16175255200; Email: udettmer@bwh.harvard.edu

Abstract

α-Synuclein (αS) forms round cytoplasmic inclusions in Parkinson's disease (PD) and dementia with Lewy bodies (DLB). Evidence suggests a physiological function of αS in vesicle trafficking and release. In contrast to earlier tenets, recent work indicates that αS normally exists in cells in a dynamic equilibrium between monomers and tetramers/multimers. We engineered αS mutants incapable of multimerization, leading to excess monomers at vesicle membranes. By EM, such mutants induced prominent vesicle clustering, leading to round cytoplasmic inclusions. Immunogold labeling revealed abundant αS intimately associated with vesicles of varied size. Fluorescence microscopy with marker proteins showed that the αS-associated vesicles were of diverse endocytic and secretory origin. An αS '3K' mutant (E35K + E46K + E61K) that amplifies the PD/DLB-causing E46K mutation induced αS-rich vesicle clusters resembling the vesicle-rich areas of Lewy bodies, supporting pathogenic relevance. Mechanistically, E46K can increase αS vesicle binding via membrane-induced amphipathic helix formation, and '3K' further enhances this effect. Another engineered αS variant added hydrophobicity to the hydrophobic half of αS helices, thereby stabilizing αS-membrane interactions. Importantly, substituting charged for uncharged residues within the hydrophobic half of the stabilized helix not only reversed the strong membrane interaction of the multimer-abolishing αS variant but also restored multimerization and prevented the aberrant vesicle interactions. Thus, reversible αS amphipathic helix formation and dynamic multimerization regulate a normal function of αS at vesicles, and abrogating multimers has pathogenic consequences.

†Deceased

Received: March 16, 2017. **Revised:** June 6, 2017. **Accepted:** June 8, 2017

Introduction

α-Synuclein (αS) is a highly abundant neuronal protein of 140 amino acids. Functions in synaptic vesicle trafficking and fusion have been proposed (1–7) but require further validation. In several neurodegenerative diseases, including Parkinson's Disease (PD) and dementia with Lewy bodies, a portion of αS forms insoluble neuronal aggregates in somata (Lewy bodies) and processes (Lewy neurites), with presynaptic aggregates possibly preceding somatic aggregates (8,9). Moreover, genetic evidence supports αS dyshomeostasis as a cause of PD, via missense mutations (10–16), copy number variants (17,18) or upregulated expression (19).

The longstanding assumption that virtually all physiological αS occurs as a natively unfolded monomer has been challenged in recent years. Unexpected findings from our (20–24) and other laboratories (6,25–29) have shed new light on earlier observations (30) by providing evidence that αS forms physiological, α-helix-rich multimers that are distinct from pathological, β-sheet-rich aggregates (the latter are traditionally called αS oligomers). The sizing of such physiological αS multimers may vary from trimers (30) to tetramers (20,21) to octamers (28). Our cell-penetrant crosslinking of endogenous αS in intact cells, including primary neurons, trapped abundant αS in ~60 kDa species, the size of four monomers (4 × 14,502 Da = 58,010 Da) (21). We observed a pronounced sensitivity of this to cell lysis, helping to explain why prior detection of intracellular αS multimers had been elusive. This lability suggested to us that dynamic intracellular populations of metastable αS multimers and monomers co-exist normally (21), apparently consistent with other recent reports of metastable tetramers (25), multimers (6,29,31) or 'conformers' that may represent multimers (27).

In response to this new body of work, several labs published data supporting the earlier model of αS existing mainly as natively unfolded monomers (32,33,34). In other labs, the new 'multimer' hypothesis triggered a search for structure-function relationships between αS monomers and multimers, with a special emphasis on their proposed function in vesicle homeostasis. One study (26) found that αS monomers purified from bacteria, but not αS tetramers purified from human red blood cells, confer membrane-remodeling activity *in vitro*. The authors suggested that tetramers are likely a 'passive' cytoplasmic storage form of the protein. Another group (6) assigned a more active role to the multimers when they used fluorescent protein complementation and high-resolution confocal microscopy to demonstrate that αS multimers on the outside surface of certain vesicles are important for vesicle clustering, which the authors suggested was a means of reducing lateral vesicle diffusion. Another report (28) proposed a physiological function of multimers in SNARE complex formation and vesicle fusion, while other studies implicated vesicle binding in the initial step of αS amyloid formation (35).

Collectively, these studies suggest complex interrelationships between the normal αS multimer state, membrane binding, vesicle trafficking/fusion and pathological αS aggregation. Using rationally designed αS mutants that decrease multimer formation and increase membrane affinity, we provided evidence that is consistent with this hypothesis. Specifically, we have described αS mutants in which we modified the characteristic KTKEGV motif that is imperfectly repeated six or seven times in αS (23,24). Our mutagenesis led to αS proteins whose features differed markedly from those of wt αS. In many iterative experiments, we have found wt αS to be distributed diffusely, enriched in the PBS-soluble cytosolic fraction, and able to be crosslinked into apparent tetramers and related multimers in intact neural cells (21,23,24). In sharp contrast, KTKEGV-motif mutants such as 6 × KLKEGV (designated 'KLK') or 7 × KTKEIV ('EIV') accumulate in PBS-insoluble fractions, can no longer be trapped as multimers by intact-cell crosslinking (only monomers are recovered), and form discrete, round cytoplasmic inclusions associated with neurotoxicity (23,24). Based on our hypothesis that wt αS is normally in a complex equilibrium that includes cytosolic and membrane-associated monomers and soluble multimers, we now present evidence that our reported KTKEGV mutants may be incapable of undergoing the necessary molecular rearrangements to populate physiologic tetramer/multimer forms. Instead, these key mutants accumulate at what has often been proposed to be the target membranes of αS: small, highly curved vesicles. Our new findings raise the possibility that normal αS tetramerization/multimerization is required for αS to interact with vesicles only transiently. In contrast, prolonged αS monomer/vesicle interactions result from our multimer-abrogating mutants, thereby inducing abnormal vesicle interactions that have detrimental consequences for neurons.

Results

αS KTKEGV variants that elevate monomer levels rapidly lead to round inclusions in neural cells

αS contains six conserved 'KTKEGV' repeat motifs, plus 2–3 less conserved partial repeats (Fig. 1A, upper left panel). We previously reported (23,24) that certain mutations introduced into all relevant KTKEGV-like motifs (Fig. 1A, remaining left panels) can markedly change the protein's properties. Specifically, KTKKGV substitutions made in repeats 3, 4 and 5 ('3K'; KTKKGV in just repeat 4 is the fPD mutant E46K), a KLKEGV mutant ('KLK') present in six repeats, and a KLKEIV mutant ('EIV') present in seven repeats) all served to: i) shift the normally highly soluble (cytosolic) αS toward PBS-insoluble fractions (23,24); ii) induce acute cytotoxicity (23,24); iii) lead to round cytoplasmic inclusions (Fig. 1A); and iv) prevent αS multimerization, as shown by both fluorescent protein complementation and application of the membrane-permeant crosslinker disuccinimidyl glutarate (DSG) (23,24). A neutral variant KTKEGR ('EGR') in six repeats behaved similarly to wt αS: it was PBS-soluble, diffusely cytoplasmic, non-toxic and allowed both YFP complementation and DSG crosslinking at 60, 80 and 100 kDa multimer positions (23,24).

Based on these findings, we now sought to characterize further the inclusions formed by the αS variants and how they might be related to those other properties: lack of multimerization, reduced solubility and increased neurotoxicity. In order to generate stable reporter cell lines to quantify inclusion formation, we expressed αS C-terminal Venus-YFP fusion proteins of the above-mentioned wt, 3K, KLK, EIV and EGR mutants in M17D human neuroblastoma cells. We generated stable cell pools by Zeocin selection. Consistent with our prior results (23,24), we observed invariant inclusion formation by 3K, KLK and EIV αS, but not by wt or EGR (Fig. 1A, middle panels: 5 days after transfection). The long-term maintenance of stable 3K, KLK or EIV lines, however, was not possible, as these three mutant lines lost expression over time (Fig. 1A, right panels), presumably due to a selection advantage of cells expressing low levels of these mutants. In contrast, the wt and benign EGR mutant cells were not lost (Fig. 1A, right panels).

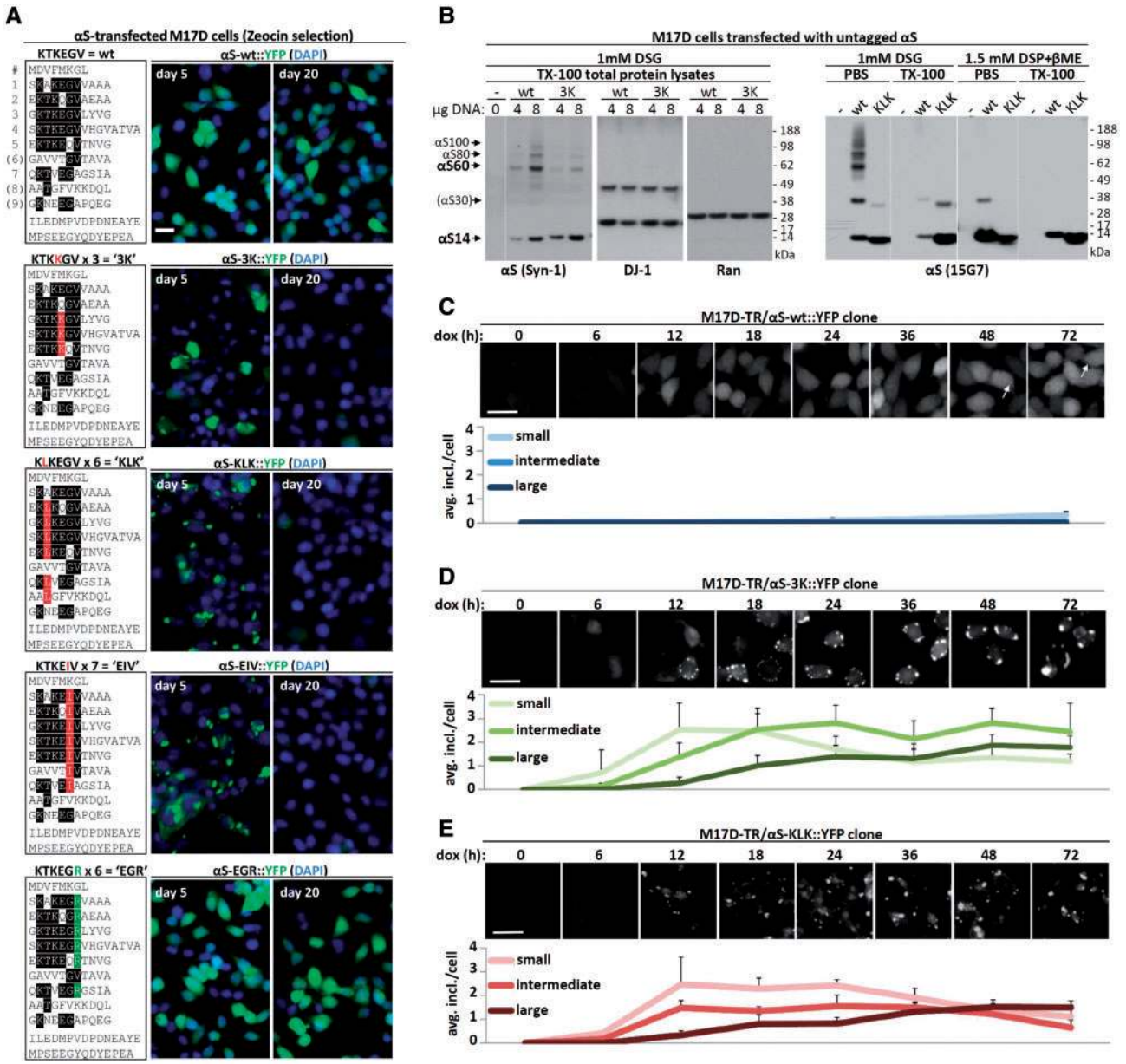

Figure 1. αS inclusion dynamics. (A) Schematics of wt αS and repeat-motif mutants by aligning aa sequences via the repeat consensus sequence KTKEGV. Middle and right panels: immunofluorescent images (YFP, green; DAPI, blue), live cells, 5 and 20 days after transfection of M17D neuroblastoma cells with the indicated αS::YFP variants followed by Zeocin selection. Scale bar, 20 μm. (B) wt vs. 3K, and wt vs. KLK αS were transiently expressed in M17D cells for 48 h followed by DSG intact-cell crosslinking and Western blot (WB). As a control, mock-transfected cells (-) are shown. Two different DNA amounts (4 and 8 μg per 6-cm dish, respectively) were transfected in the case of wt vs. 3K (left panels), total protein lysate and blots were developed for αS (mAb Syn-1), DJ-1 (dimeric protein, positive control/loading control) and Ran (monomeric protein, negative control/loading control). Wt vs. KLK (right panels, mAb 15G7) was analyzed by sequential extraction (PBS fraction, ~cytosol; TX-100 fraction) and adding DSP/βME-reversed crosslinking (see Methods) to visualize total αS amounts. Note that, consistent with earlier data, we sometimes observe αS30 putative dimers upon transient overexpression, while apparent trimers are typically absent. Data represent at least 10 independent experiments. Membranes were cut as indicated by thin white lines. (C) Time-course of αS-wt::YFP induction in a clonal cell line. M17D cells expressing YFP-tagged αS 3K (dox-inducible) were induced for the indicated time points (all cells plated at the same time, but induced at different time points), then fixed (4% paraformaldehyde) and imaged. Only very few smaller inclusions (<2 μm) were observed, mostly at later time points. This and subsequent graphs based on three independent cultures, 20 cells each. Scale bar, 20 μm. (D) Time-course of αS-3K::YFP induction in a clonal cell line. M17D cells expressing YFP-tagged αS3K (dox-inducible) were induced for the indicated time points, then fixed (4% paraformaldehyde) and imaged. Over time, the number of medium (1–2 μm diameter) and large (>2 μm) inclusions increased, at the expense of small inclusions (<1 μm). Scale bar, 20 μm. (E) Analogous to (D), but αS-KLK::YFP.

To further characterize these potentially cytotoxic (23,24) inclusions, we mainly focused on the 3K and KLK mutants. Both αS variants were confirmed to be largely monomeric by intact-cell crosslinking with 1 mM DSG of the M17D transfectants followed by Western blot (WB) with different antibodies (Fig. 1B), as expected from our prior work (23,24). For αS 3K (Fig. 1B, left half), only small amounts were trapped by DSG at the putative tetramer (60 kDa, called αS60) and dimer (30 kDa, called αS30) positions. For αS KLK (Fig. 1B, right half), αS60 was entirely abolished; only trace amounts of dimer (αS30) in addition to

abundant monomers (αS14) were present. The wt αS transfectants contained abundant αS multimers at αS60 (putative tetramer), αS80 (80 kDa) and αS100 (100 kDa) positions. We have hypothesized that αS80 and αS100 represent hexamers and octamers or alternatively are distinct native tetramer conformations that are trapped slightly differently by the DSG (*i.e.* they are conformers) (21). In addition, wt αS populated some putative dimers (αS30). We previously documented that the dimers are almost absent with *endogenous* wt αS but occur to a variable degree with *overexpressed* wt αS (see, *e.g.* Fig. 3A in (21)). We previously excluded that the species described here are αS heteromultimers with other αS-binding proteins by using co-IP, 2D gel electrophoresis (21) and mass spectrometry (23). The current data thus support that wt αS forms abundant multimers, principally tetramers, in intact neural cells, whereas the αS 3K and KLK mutants populate overwhelmingly monomeric species. This apparent stabilization of αS in a monomeric state promised to be of value in our quest to explore αS structure-function (and dysfunction) relationships.

To overcome the loss of 3K and KLK expressing cells over time, we isolated the doxycycline (dox)-inducible clonal lines M17D-TR/αS-wt::YFP, M17D-TR/αS-3K::YFP and M17D-TR/αS-KLK::YFP, and collected fluorescent images over an induction time course. Only very few inclusions, which were small and not bright, developed in the control M17D-TR/αS-wt::YFP cells (Fig. 1C). For 3K and KLK, diffuse YFP signal became visible as soon as 6 h after dox-induction, and initial inclusions appeared as soon as 12 h post-dox (Fig. 1D and E). We categorized inclusions into three size groups (<1, 1–2 and >2 μm in diameter) and observed a trend of increasing inclusion size and decreasing inclusion number between 12 and 72 h, suggestive of fusion events over time (Fig. 1D and E). A portion of the 3K, and even some of the KLK, signal remained diffusely cytosolic (Fig. 1D and E), like almost all the wt signal (Fig. 1C).

The αS cellular inclusions are rich in vesicles

To further analyze the inclusions caused by 3K and KLK expression, we induced M17D-TR/αS-3K::YFP cells for at least 24 h and imaged them by immuno-electron microscopy (EM). In the analyzed cells, we observed round zones in the cytoplasm (Fig. 2A, middle panel, boxed) that were more electron-dense than the surrounding cytoplasm and had the approximate diameters of the large YFP inclusions seen by light microscopy in living cells (Fig. 2A, top panel). Immunogold labeling for YFP (Fig. 2A, black dots in middle and bottom panels) confirmed that these structures were rich in αS-3K::YFP, and higher magnification (Fig. 2A, bottom right panel) identified vesicular (arrowheads) and tubular (arrows) membranous structures as principal components. In the absence of dox-induction (Fig. 2B), no inclusions were seen by either fluorescence microscopy or EM, and immunogold labeling was virtually absent. Immunogold labeling of the induced cells for αS (pAb C20; Fig. 2C) confirmed the co-localization of multiple vesicles (arrowheads), tubules (arrows) and αS (black dots) within the spherical inclusions. Stronger image contrasting in the absence of immunogold (Fig. 2D) allowed even better visualization of myriad round vesicles (arrowheads) and elongated tubules (arrows) within the cytoplasmic inclusions. Another consistent finding in many but not all cells analyzed were large vacuoles with an electron-lucent center and a ~0.5–2 μm in diameter in close proximity to the inclusions (asterisks in Fig. 2A, C and D). Their size and appearance (the jagged perimeters are likely an artifact of fixation) are consistent with lipid droplets.

As a control, dox induction of wt αS::YFP (*i.e.* in M17D-TR/αS-wt::YFP cells) produced only diffuse cytoplasmic YFP signals (Fig. 3A, top panel), consistent with diffuse immunogold labeling for YFP (middle panel) or αS (pAb C20, bottom panel). In contrast, the multimer-abolishing variants αS EIV (Fig. 3B; see Fig. 1A for its sequence) and αS KLK (Fig. 3C) had YFP+ and αS+ inclusions (note that EIV was studied in epon sections, KLK in frozen sections). Interestingly, we observed a variety of different membranous structures in the inclusions, ranging from clusters of vesicles of different diameters (*e.g.* EIV: Fig. 3B middle panel) to pronounced tubular structures (*e.g.* EIV: Fig. 3B bottom panel), and these could co-exist in the same cells. Moreover, the consistent position of the immunogold particles relative to the vesicles (*e.g.* EIV: Fig. 3B middle panel) suggested that αS is localized on but not inside vesicles.

αS-rich inclusions contain vesicles of diverse origins

To identify the origin of the vesicles that cluster with the multimer-abolishing αS variants, we transfected the 3K::YFP and KLK::YFP inducible lines with various constitutively expressed marker proteins that were tagged with red fluorescent protein (RFP). As a first step, we transfected RFP alone into M17D parental cells as well as into the inducible lines αS wt::YFP, 3K::YFP and KLK::YFP (Fig. 4A) and waited for stable RFP cDNA integration in the cell pool. After inducing the αS transgenes, we observed diffuse co-localization of wt αS with RFP, as expected. The inclusions that were invariably formed in the case of 3K and KLK, however, did not trigger analogous local accumulations of the RFP protein; it remained diffuse (Fig. 4A). Next, we co-expressed a variety of RFP-tagged membrane marker proteins together with αS 3K::YFP (Fig. 4B) or KLK::YFP (data not shown). To better model the steady-state situation, we again waited for stable integration of these transgenes to occur and examined a pool with a relatively low percentage of double-positive cells. In 'blinded' cultures, we identified those cells that had inclusions and were clearly both YFP- and RFP-positive. Next, we asked whether the αS::YFP inclusions in such double-positive cells were themselves also RFP-positive. We observed at least one such double-positive inclusion in 100% of inclusion-bearing cells co-expressing the RFP-tagged endosomal markers transferrin receptor, RHOB (Ras homology family member B), Rab5, Rab7 and Rab11 (Fig. 4B; see legend for further details). The autophagosomal marker Lamp1 (91.7 ± 7.2% double-positive cells with punctate colocalization) and the Golgi marker sialyltransferase (SiT; 87.5 ± 10.2%) co-localized with the αS-rich inclusions, as well (Fig. 4B). In contrast, the signals from RFP-labeled ER (Calreticulin, Crt; 8.3 ± 7.2%) or mitochondrial (cytochrome c oxidase subunit 8A, COX8A; 4.2 ± 7.2%) markers spared the areas of αS inclusions, just like RFP alone (4.2 ± 7.2%). Based on this observation, we reasoned that pharmacological inhibition of pathways that produce cellular vesicles may reduce the inclusion formation. We thus treated the cell line M17D-TR/αS-3K::YFP//RFP (which also stably expressed RFP for normalization) with DMSO vehicle only, or the endocytosis inhibitor dynasore, or brefeldin A, which inhibits vesicle transport from ER to Golgi. IncuCyte-based automated image analysis of YFP (only punctate signals taken into account) and RFP (pan-cellular signal) revealed that both drugs modestly but significantly reduced inclusion formation (Fig. 4C: see bar graphs and legend for quantification). In contrast to our transient transfections (23,24), the cultures exhibited only minor acute toxicity when αS expression was induced in the αS 3K or αS KLK inducible lines

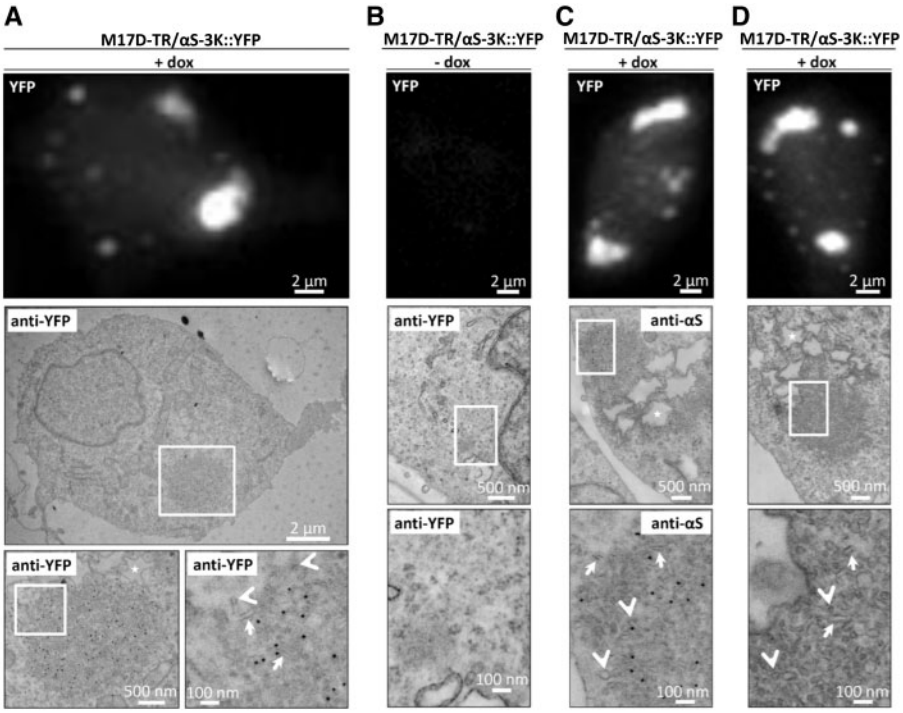

Figure 2. Ultrastructure of αS-3K::YFP inclusions in induced M17D cells. (**A**) YFP fluorescence (top panel) and immunogold EM images (middle and bottom panels; bottom panels are zoom-in images as indicated) of M17D-TR/αS-3K::YFP cells that were dox-induced for 48 h. Anti-YFP antibodies were used for immunogold labeling (15 nm particles) of epon sections. Arrows point at vesicular, arrow heads at tubular structures, asterisks mark lipid-droplet-like structures. This and subsequent figures (**B–D**) represent four independent experiments. (B) Analogous to (A), but non-induced cells. (C) Analogous to (A), but anti-αS (pAb C20). (D) analogous to (A), but without immunogold. All scale bars as indicated.

(not shown). In this context, we observed that the 3K::YFP and KLK::YFP expressing M17D cells were still able to undergo mitosis, during which the inclusions were still present in daughter cells but visibly rearranged (Fig. 4D and E). To validate the above findings in the absence of fluorescent protein tags, we generated inducible cell lines for untagged αS wt (M17D-TR/αS-wt) and αS KLK (M17D-TR/αS-KLK). WB confirmed the induction of transgene expression only in the presence of dox (Fig. 5A). Immunofluorescence (IF) using antibodies specific for αS (pAb C20) and transferrin receptor revealed strong co-localization of αS KLK, but not αS wt, with putative endosomal vesicles containing transferrin receptor (Fig. 5B). This was confirmed for KLK αS (Fig. 5C, right panel) but not for wt αS (left panel) by performing co-fractionation with transferrin receptor by non-denaturing size-exclusion chromatography. In this experiment, the cell lysates were prepared from the induced lines by passing through a 16G needle 20 times and in the absence of detergent in order to leave most vesicles intact. Subsequent IF microscopy of the αS KLK line revealed pronounced co-localization with a variety of other vesicular markers (Fig. 5D), from left to right: Rab5 (early endosome), Rab7 (late endosome), Rab11 (recycling endosome), Lamp1 (lysosomal/autophagosomal) and Giantin (Golgi). In contrast, we did not observe major overlap with ER membranes (marked by Calnexin: Fig. 5D, third panel from right) or mitochondria (TOM20: second panel from right). In agreement, iodixanol gradients of total protein lysates separated αS KLK protein (Fig. 5E, right panel) from the dense ER membranes (marker: calnexin). Conversely, αS KLK co-fractionated with the vesicular markers transferrin receptor and Lamp1. As expected, wt αS (Fig. 5E, left panel) mainly co-fractionated with GAPDH in the top (cytosolic) fractions of the iodixanol gradient.

3K and KLK αS proteins accumulate at synaptic vesicles in neurons

Similar to M17D human neuroblastoma cells, lipofection of 3K::YFP into primary neurons time-dependently induced round, punctate inclusions (Fig. 6A, lower panels, arrows indicate puncta) in somata and neurites that increased in size over time, whereas wt αS remained diffuse or else small, focal accumulations were mostly transient and disappeared (Fig. 6A, upper panels). Around 48 h post-transfection, the occurrence of cells with defined round somatic or neuritic inclusions was strongly increased (Fig. 6A, quantification on the right) for 3K (75.3 ± 4.5% of cells) compared to wt (6.7 ± 0.7% of cells). This focal accumulation of 3K αS was often accompanied by evidence of gradual cytotoxity such as rounded cell bodies seen by 60 h (Fig. 6A, arrowhead). Interestingly, we observed that αS-3K::YFP accumulations were apparently able to 'seed' the accumulation of co-transfected αS-wt::RFP into the focal puncta (Fig. 6B, fourth column), whereas this co-localization did not occur with co-transfected RFP alone (Fig. 6B, third panel). This co-accumulation phenomenon was seen in both somata (arrows) and neurites (arrowheads) (Fig. 6B, fourth panel; magnified in fifth panel). In the same experiments, αS-wt::YFP and RFP (Fig. 6B, first panel) or αS-wt::YFP and αS-wt::RFP (Fig. 6B, second panel) just co-localized diffusely throughout the cytoplasm.

Importantly, in the absence of fluorescent protein tags, IF of untagged αS 3K and KLK expressed in primary mouse neurons also showed punctate inclusions (Fig. 6C, middle and bottom row, left panel) whereas αS wt expression remained diffuse (Fig. 6C, top row, left panel). Consistent with the vesicular localization of 3K and KLK in the neuroblastoma lines, we found strong co-localization in the primary neurons of both mutant αS forms with

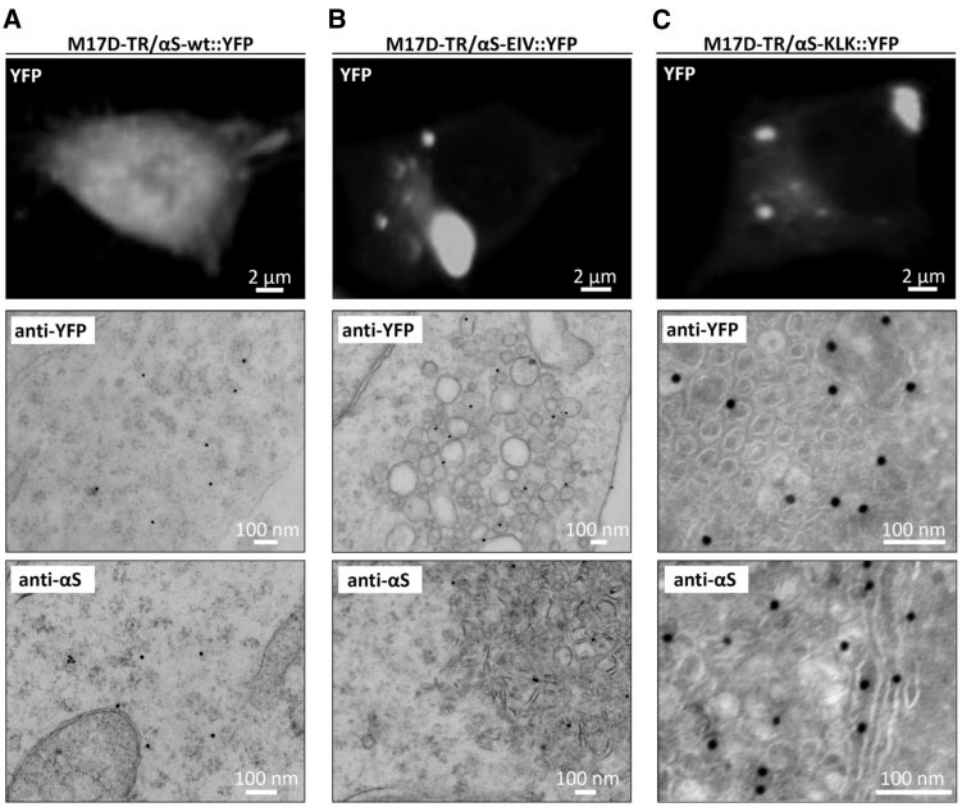

Figure 3. Ultrastructure of αS-wt::YFP, -EIV::YFP, -KLK::YFP inclusions in induced M17D cells. (**A**) YFP fluorescence (top panel) and immunogold-EM images (middle and bottom panel) of M17D-TR/αS-wt::YFP cells that were dox-induced for 48 h. Anti-YFP (middle panel) and anti-αS (bottom panel) antibodies were used for immunogold labeling (15 nm particles) of epon sections. Representative of three experiments. (**B**) Analogous to (A), but αS-EIV::YFP. Anti-YFP images were selected to show more vesicle-like, anti-αS images to show more tubule-like structures, but both structures were found in all cultures tested; representative of four experiments. (**C**) Analogous to (A), but αS-KLK::YFP and frozen instead of epon sections; representative of four experiments. All scale bars as indicated.

the synaptic vesicle marker synaptophysin, while such punctate co-localization was less pronounced for wt (Fig. 6C). These observations were then corroborated by IF and parallel immunogold-EM analysis of lentivirus-transduced primary mouse neurons (infection on DIV7, fixation on DIV14; Fig. 6D): transduced αS wt (Fig. 6D, top right panel) was found in both vesicle-rich areas (arrows in EM images) and other parts of neurites (arrowheads in EM images), whereas αS 3K (Fig. 6D, bottom left panel) and KLK (bottom right) were almost exclusively associated with vesicles, apparently in boutons. Empty-vector treated neurons (Fig. 6D, top left panel) showed only a few, scattered gold particles, confirming that most of the observed αS gold signals in the transduced neurons were indeed due to expression of the transgene. Quantification of gold particles as vesicle-associated vs. 'free' confirmed a significant redistribution to vesicles for αS 3K and KLK vs. wt (Fig. 6E and F). Of note, the endogenous mouse αS exhibited a similar diffuse staining as transduced wt human αS. Similar to results in the neuroblastoma cells, this non-transient expression of each of the αS variants was not accompanied by an obvious time-dependent neuronal loss. To search for subtler effects of the αS variants, we monitored neurite outgrowth by unbiased automated quantification (IncuCyte) in the transduced mouse neurons and observed a significant ~20% reduction in neurite length for αS 3K (80.8 ± 13.6% of wt neuron length) and KLK (81.7 ± 11.2% of wt neuron length) 96 h post-transduction of DIV2 neurons (Fig. 6G: representative time-course experiment; Fig. 6H: quantification of neurite length 96 h post-transduction; see figure legend for details).

Molecular mechanism: abnormally stabilized αS amphipathic helices underlie the strong αS-membrane interactions and aberrant vesicle interactions of the multimer-abrogating mutants

Based on a helical wheel model of αS amphipathic helix formation *in vitro* (*e.g.* Fig. 1 of (5)), we hypothesized that our inclusion-promoting αS variants (3K, KLK, EIV) abnormally stabilize α-helical αS monomers at membranes (see Fig. 7 for model). It is believed that the 11-residue repeats having the core motif KTKEGV enable αS to transiently and dynamically interact with the outer surface of curved membranes (5). Especially when lipid packing defects occur in such membranes, αS binding was reported to induce an amphipathic helix whose hydrophobic half is buried in the outer leaflet of the lipid bilayer (36–38), while the hydrophilic half is exposed to the aqueous environment of the cytoplasm.

In addition, positively-charged lysine residues on the hydrophilic face of each repeat motif helix are believed to interact with negatively charged lipid headgroups of vesicles (39). Due to the occurrence of several polar (threonine) or small (glycine) residues in the hydrophobic half of each repeat motif, the hydrophobic interactions between wt αS and the lipid bilayer can be considered relatively weak (Fig. 7A). This may explain why wt αS is largely a soluble, cytosolic protein, with only 10–20% of it associated with membranes (40,41). Our strongly inclusion-promoting αS repeat mutants KLK and EIV have increased hydrophobicity in the hydrophobic half of the helix (Fig. 7C and D). This would lead to a more energetically stable amphipathic

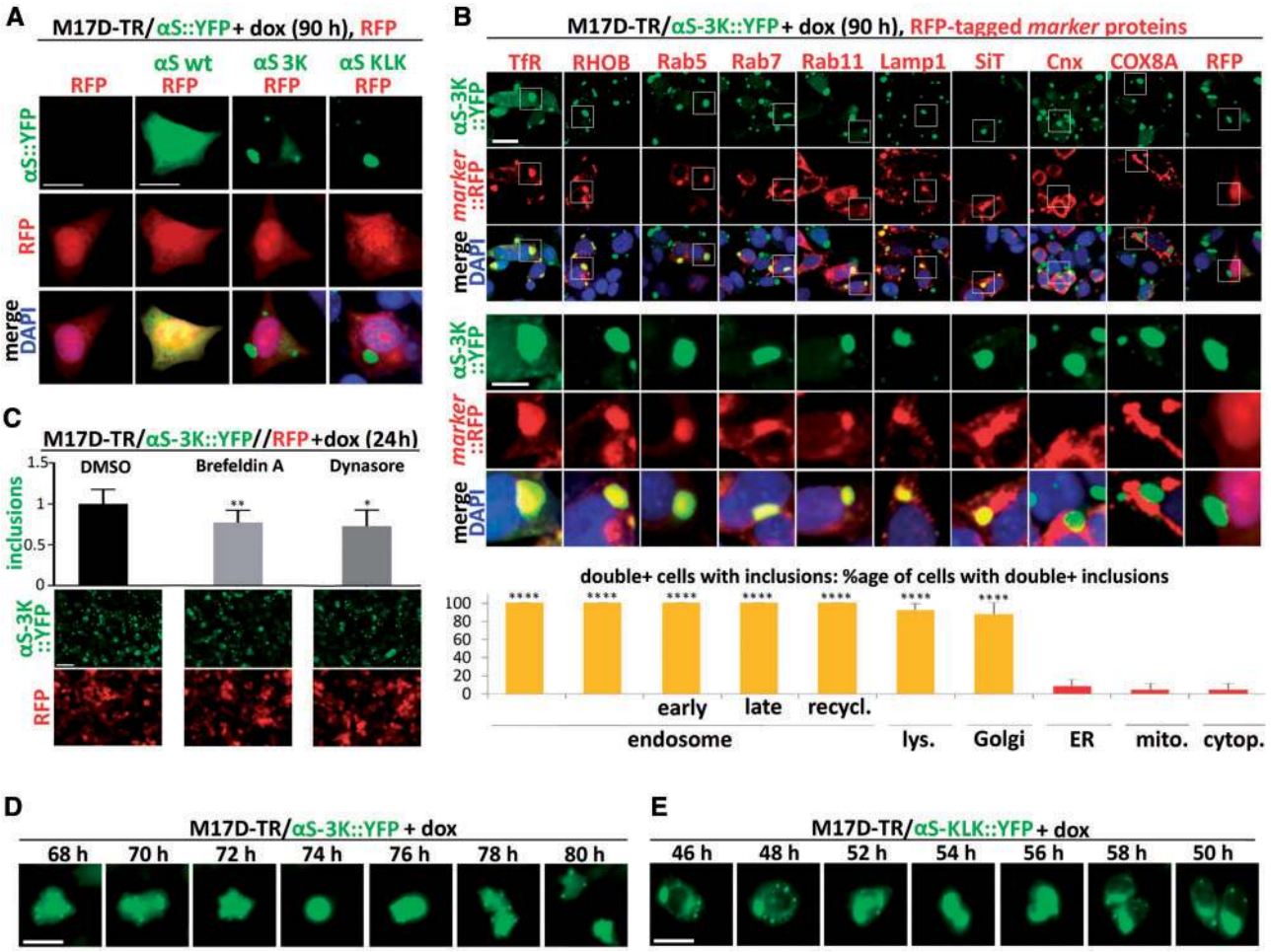

Figure 4. αS-3K::YFP inclusions colocalize with endosomes, lysosomes, and Golgi components in induced M17D cells. (**A**) Parental M17D cells or M17D-TR cells expressing YFP-tagged αS wt, 3K or KLK were transfected with cDNA for RFP and passaged for 10 days to achieve stable RFP expression in a subset of cells. Then αS expression was induced by dox for 90 h. Fluorescence microscopy for YFP (top), RFP (middle) plus merge images that include DAPI staining for nuclei (bottom). Scale bar, 10 μm. (**B**) Analogous to (A), but stable expression of RFP or indicated RFP-tagged markers in M17D-TR/αS-3K::YFP cells. Statistics were generated by first identifying inclusion-bearing double-positive (YFP and RFP) cells and then assigning '1' to cells with apparent colocalization in at least one round inclusion and '0' to cells without distinct colocalization in round inclusions. Samples were blinded during analysis. Three independent experiments, eight double-positive inclusion-bearing cells each ($N = 3$, $n = 24$); significance relative to RFP alone. Scale bars, 10 μm and 5 μm (zoom-in), respectively. (**C**) IncuCyte-based quantification of integrated YFP inclusion intensity and total RFP in induced (24 h) M17D-TR/αS-3K::YFP//RFP cells, plus representative images. 0.1% DMSO (vehicle), 300 μM brefeldin A and 80 μM dynasore were applied shortly after induction. Inclusion integrated intensities relative to DMSO (whose mean was set to 1 in each experiment) were 77.2 ± 15.0% (brefeldin A) and 73.2 ± 19.6% (dynasore). Three independent experiments in triplicates ($N = 3$, $n = 9$), significance relative to DMSO only. Scale bar, 50 μm. Integrated intensities of co-expressed RFP were not significantly changed. (**D**) Time-course of induced M17D-TR/αS-3K::YFP. IncuCyte analysis, YFP images were were taken in 2h intervals up to 96 h after induction, revealing mitotic events within this time frame for both 3K- and KLK-expressing cells. Scale bar, 10 μm. (**E**) Analogous to (D), but M17D-TR/αS-KLK::YFP. One-way ANOVA for statistical analyses. Bars are means +/− S.D. Criteria for significance: $^{*}P < 0.05$, $^{**}P < 0.01$, $^{***}P < 0.001$, $^{****}P < 0.0001$.

helix and thus account for an enhanced binding to cytoplasmic vesicles, consistent with the increased occurrence of αS EIV and KLK in buffer-insoluble fractions of sequential extracts that we observe (24). For αS 3K (Fig. 7B), this enhanced membrane interaction (23) may be due to the additional positive charges in the hydrophilic half of the helix, which can interact with negatively charged lipid headgroups, as has been reported for the E46K fPD mutation alone (42).

Based on the above considerations, we reasoned that weakening the membrane-induced αS amphipathic helices in our mutants might reverse the observed effects of 3K, KLK and EIV αS. To this end, we introduced additional energetically unfavorable arginines (positive charges) into the hydrophobic half of the abnormally stabilized αS KLK amphipathic helix, generating a compound mutant with the consensus sequence KLKEGR (Fig. 8A–C, bottom). Strikingly, this variant reversed the strong membrane association of αS KLK (Fig. 8D, middle): KLKEGR showed a strong cytosolic enrichment (Fig. 8D, bottom), similar to wt (Fig. 8D, top). Importantly, this restored solubility was accompanied by restored αS60/80/100 multimer formation, as tested by crosslinking (Fig. 8E, bottom, vs. the mostly monomeric KLK) and a restored diffuse cytosolic distribution upon expression in rodent neurons (Fig. 8F, bottom, vs. the focal accumulation of KLK).

Discussion

αS is the principal misfolded protein that accumulates progressively in a group of fatal neurodegenerative diseases, including PD, dementia with Lewy bodies, multiple system atrophy, and to a lesser degree in Alzheimer's disease. Accordingly, it is critical to understand the mechanisms that initiate αS accumulation in round insoluble cytoplasmic

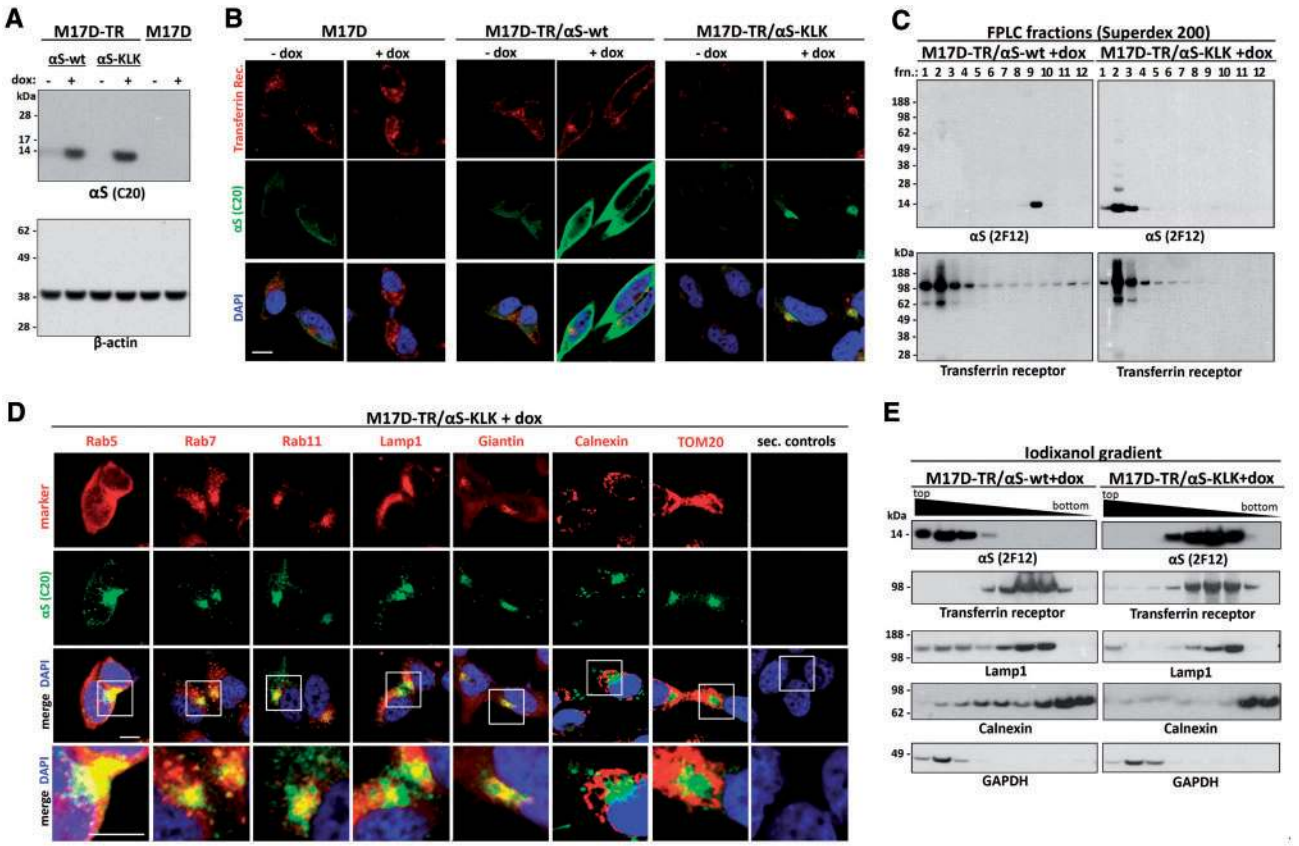

Figure 5. Untagged αS KLK colocalizes and cofractionates with endosomal, lysosomal and Golgi components in induced M17D cells. (**A**) Parental M17D or dox-inducible M17D-TR/αS-wt and -KLK cells were induced for 48 h (+dox) or not (-dox). αS (pAb C20) WBs for total protein lysates (1% Triton-X 100), control WB for β-actin. WB represents five experiments. (**B**) Same cell lines and induction as in (A), IF images for transferrin receptor (TfR mAb, red) and αS (αS C20 pAb, green), plus merge images that include DAPI to visualize nuclei. Scale bar, 5 μm. (**C**) Size-exclusion chromatography (Superdex 200). Cells were lysed by needling, and post-nuclear supernatants were separated into 12 fractions that were collected and analyzed by WB for αS and TfR (representative blots of two independent experiments). (**D**) M17D-TR/αS-KLK cells were induced for 48 h. IF microscopy for the indicated marker proteins (specific antibodies, red), αS (pAb C20, green) plus merge images that include DAPI staining (bottom row: zoom-in images as indicated). Right panels: secondary antibody only controls. Scale bar, 5 μm. Data represent at least three independent experiments per marker protein. (**E**) Iodixanol density gradient centrifugation using total protein lysates of M17D-TR/αS-wt and -KLK cells ($N = 3$). Fractions were analyzed by WB for αS (2F12), TfR (endosome), Lamp1 (lysosome), Calnexin (ER) and GAPDH (soluble). Top fractions contain soluble proteins, bottom fractions contain the cellular membranes of the highest density (mostly ER).

inclusions in these disorders and to establish controlled experimental systems to model this process, in order to screen for compounds that could restore normal αS homeostasis. To these ends, we report detailed analyses of a new model for the controlled formation of round cytoplasmic αS inclusions associated with neurotoxicity. In our initial work on this model (24), we engineered certain KTKEGV repeat-motif mutations that abolished the abundant ~60 kDa assemblies we normally observed with wt αS upon intact-cell crosslinking. We reported that the loss of the 60 kDa assembly caused by these αS mutations was accompanied by neurotoxicity, and the resultant αS proteins were largely insoluble and led to multiple, round cytoplasmic inclusions. In the current study, we analyze two such repeat-motif mutants in depth in order to systematically characterize the striking inclusions they form: a) αS 3K (E35K + E46K + E61K) that represents an amplification of the fPD-linked mutant E46K into the two adjacent KTKEGV motifs; and b) an engineered mutant that changes the KTKEGV core motif to KLKEGV in six repeats.

By studying both variants in several neuronal systems, we show that the round cytoplasmic inclusions arising from these KTKEGV motif mutations are comprised of clusters of vesicles and tubules intimately associated with the focal accumulation of αS (see the immunogold EMs of Figs 2, 3 and 6). Dense clusters of vesicles shown to be derived from diverse subcellular membranes (endocytic, lysosomal, Golgi) developed in the cytoplasm of human neural cells upon expression of αS 3K or KLK (Figs 4 and 5). Based on a previous study that analyzed a KLK-like αS variant *in vitro* and in yeast (43), we expected our αS variants to potentially interact with membranes besides those of small vesicles, but we found no evidence for appreciable interactions with non-vesicle membranes such as mitochondria and ER. Cytotoxicity, which is typically pronounced when we express mutants like 3K and KLK transiently at high concentrations (23,24) (Fig. 1A), was less severe when the expression was stable and chronic, perhaps due to lower expression levels, the absence of lipofection, and/or compensatory cellular mechanisms developing over time. Nonetheless, we were unable to generate stably expressing αS 3K or KLK neuroblastoma cells, and we observed reduced overall neurite length in transduced neuronal cultures expressing the 3K or KLK mutants for several days (Fig. 6G and H). These results suggest that the accumulation of multimer-abrogating KTKEGV motif mutants interferes with vital cellular processes.

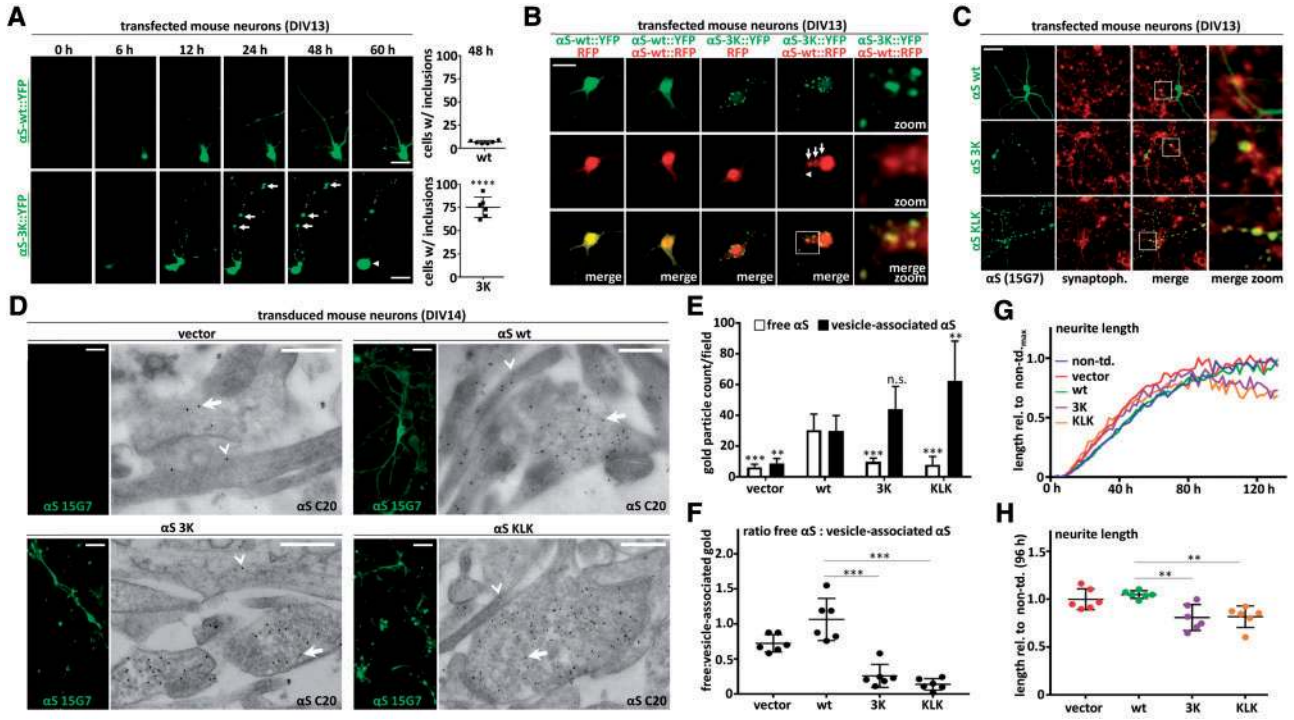

Figure 6. αS 3K and KLK are closely associated with vesicles in primary neurons. (**A**) Time course αS-wt::YFP and αS-3K::YFP transfection in DIV13 primary mouse cortical neurons. IncuCyte fluorescence microscopy. Arrows indicate larger neuritic inclusions that increase in size over time. Data are representative of three independent experiments done in triplicate ($N = 3$, $n = 9$). For quantifications at 48 h post transfection, 100 cells per experiment were analyzed and '1' was assigned to cells with at least one large (> 2 μm) round focal αS accumulation and '0' to cells without. Images were blinded during analysis. Scale bar, 20 μm. (**B**) Colocalization analysis of αS-wt::YFP with RFP and αS::RFP as well as αS-3K::YFP with RFP and αS-wt::RFP in transfected neurons (48 h post transfection). Autofluoresence in fixed cells: YFP, RFP and merge images. Arrows indicate αS-wt::RFP signals that co-localize with 3K:YFP in inclusion-like structures. Scale bar, 20 μm. Data represent three independent experiments. (**C**) Colocalization analysis of untagged αS wt, 3K and KLK in transfected neurons (48 h post transfection). Fluorescence microscopy for αS (human-specific mAb 15G7) and synaptophysin plus merge images (same scale and zoom-in). Data represent three independent experiments. Scale bar, 20 μm. (**D**) IF and EM analysis of mouse neurons transduced with vector, wt, 3K and KLK αS on DIV7 and fixed on DIV14. IF images (human-specific αS mAb 15G7) on the left, anti-αS immunogold EM (pAb C20, detects both endogenous and transduced human αS; 15 nM particles; epon sections) on the right of each panel. Arrows indicate vesicle-associated, arrowheads free gold particles. Scale bars, 20 μm (IF) and 500 nm (EM). Data represent two independent experiments. (**E**) Quantification of vesicle-associated vs. free αS for EM pictures shown in d). Three fields each from two independent experiments ($N = 2$, $n = 6$) were analyzed (blinded counting). (**F**) Ratios calculated from quantifications in (E). (**G**) IncuCyte-based analysis of neurite outgrowth as a measure of non-overt neurotoxicity. Cells were transduced on DIV2 with virus (or not) as indicated. Imaging started after infection, starting values were set to 0. All values were normalized to the neurite length of non-transduced neurons, which was set to 1. Representative of three independent experiments done in duplicates. (**H**) Quantification of neuron length 96 h post transduction. All values were normalized to the neurite length of non-transduced neurons, which was set to 1. Three independent experiments were done in duplicates ($N = 3$, $n = 6$). Significance αS 3K and KLK relative to αS wt-transduced neurons. One-way ANOVA for all statistical analyses, except 6(A) (unpaired t-test, two-tailed). Means +/− S.D. Criteria for significance: $^{*}P < 0.05$, $^{**}P < 0.01$, $^{***}P < 0.001$, $^{****}P < 0.0001$.

The vesicle clusters that we observe are reminiscent of the effects of expressing human αS at relatively high concentrations in *S. cerevisiae*. After these αS inclusions in yeast had initially been interpreted by light microscopy as proteinaceous aggregates, Soper et al. instead provided ultrastructural evidence that αS accumulations in yeast were not comprised of fibrils but rather were clusters of many vesicles (44). Similarly, Gitler et al. observed in yeast the accumulation of undocked vesicles coalescing into massive intracellular vesicular clusters in a wt αS dose-dependent manner (45). By IF and immuno-EM, these yeast inclusions were associated both with αS and vesicle markers of diverse subcellular origin (endosomes, Golgi, lysosomes), closely similar to the marker co-localization data in our 3K and KLK αS transfectants (Figs 4 and 5). In contrast to yeast expressing wt human αS, mammalian cells expressing very high levels of wt or even fPD single-mutant αS (*e.g.* E46K) still have the protein in a highly soluble state, without discrete inclusion formation (23,24,46,47). Our new data herein indicate that the strong vesicle-aggregating property of human αS is not unique to yeast but can also be achieved in mammalian neurons if the αS sequence is altered in ways that move the tetramer/multimer-to-monomer equilibrium strongly toward excess monomers. As far as αS physiology is concerned, the trafficking and clustering of vesicles within synaptic terminals has been suggested to be a normal function of αS (1–7). This raises the possibility that the abnormal vesicle clustering we find to be caused by KTKEGV mutants is a form of excessive αS function. Importantly, the inclusion propensity of wt αS is not zero (Fig. 1C), indicating that our αS mutants may augment an intrinsic feature of the wt protein. In this scenario, αS 3K and αS KLK can be considered dominant active (or constitutively active) proteins. Interestingly, a study (26) reported the membrane-remodeling activity of membrane-associated monomeric αS, and the authors suggested that αS tetramers in the cytosol (which they successfully prepared from fresh erythrocytes) was not active in their assay and thus might represent an "inactive storage form" of the protein. We identified the KLK, 3K, EIV and EGW repeat-motif mutations because of their inability to form and maintain cytosolic αS tetramers/multimers (23,24).

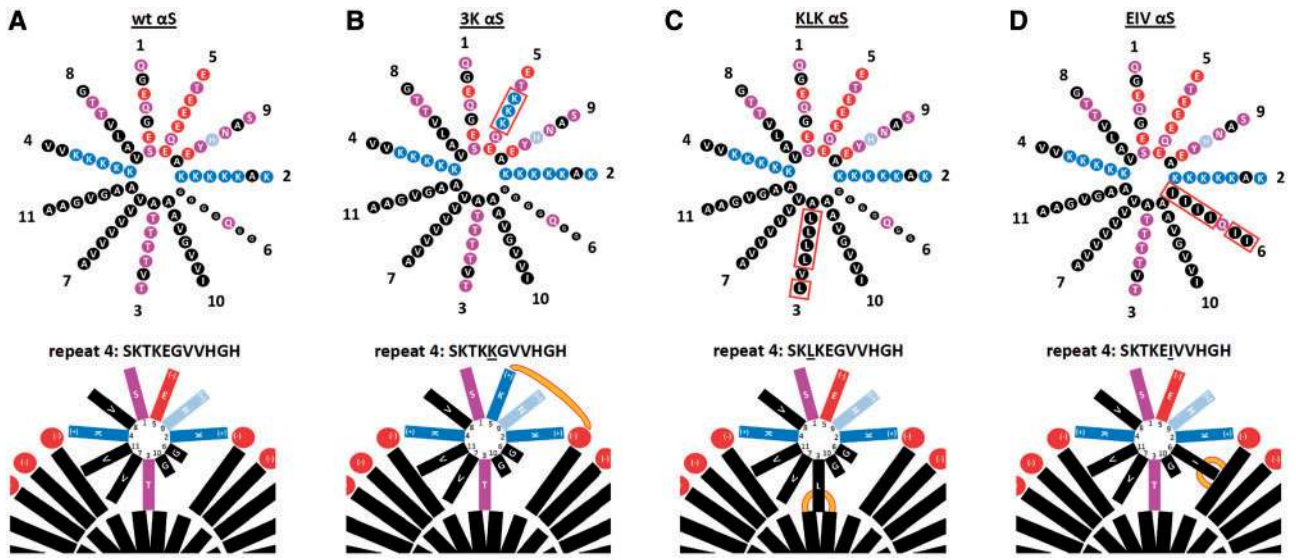

Figure 7. Wt αS forms a normally dynamic membrane-induced amphipathic α-helix. (**A**) Top: wt αS contains at least seven 11-residue repeats (1–5 and 7 being highly conserved) arranged in a helical wheel (a 3–11 helix: 3 turns over eleven residues). Blue indicates basic (light blue: histidine), red: acidic, purple: polar uncharged, and black: non-polar residues. Bottom: Schematic of αS repeat #4 embedded in the outer leaflet of a curved vesicle membrane (lipid head-groups in red, fatty acid 'tails' in black). Hydrophobic interactions between non-polar residues and the lipid environment as well as electrostatic interactions between positively charged lysine-residues (blue) and negatively charged lipid headgroups (red) are proposed to stabilize the amphipathic helix transiently. (**B–D**) Analogous to (A), but for 3K, KLK and EIV αS. Note that KLK has a distal T92L mutation that is not depicted here (see Fig. 1A). Orange lines illustrate increased αS-membrane attraction.

Taken together, these various considerations support a hypothetical model (Fig. 9) in which wt αS is translated on the ribosome as an unfolded monomer (A) that then rapidly binds to the external surfaces of certain curved vesicle membranes in the crowded cytoplasm and adopts helical folding (B1), thereby promoting vesicle clustering to a limited extent. The αS-vesicle interactions could weaken when αS monomers normally multimerize (B2), as we recover multimers overwhelmingly from the cytosol (21,23). Metastable soluble multimers are likely to disassemble in the cytosol over time (B3), starting a new dynamic cycle (B1'-B3'). For our KTKEGV mutants 3K, KLK and EIV (C1–C4), this cycle could be impaired: after translation and membrane binding (C1), they are presumably unable to undergo normal multimerization, prolonging their membrane association as monomers and intensifying the vesicle-clustering effect (C2). The acute/subacute consequences may be defects in vesicle trafficking and membrane rearrangements such as the tubulation we observe (C3). A longer-term consequence may well be the coming together of the excess monomers to form β-sheet-rich αS aggregates (C4; see next paragraph). Excess wt αS monomers (D1–D4) as caused by SNCA gene duplication/triplication may result in similar defects due to shifting the normal tetramer:monomer equilibrium toward free monomers by titrating out a limiting factor (*e.g.* arachidonic acid or another small lipid (29)) that helps assemble and transiently stabilize multimers (D2).

In this combined model, physiological αS tetramers/multimers could serve the purpose of a) limiting αS monomer functional activity at membranes; and b) storing αS in a non-aggregation-prone form (20) in the cytoplasm. Further studies will be necessary to elucidate how αS switches between monomeric vs. multimeric and between cytosolic vs. membrane-bound states and how this dynamic behavior regulates normal αS function in vesicle trafficking/fusion. The mutants that we describe should be valuable tools, as they can be considered loss-of-function for normal αS multimerization, and the resultant excess monomers may be dominant-active with regard to αS function at vesicles. If the apparent monomeric nature of our αS variants in the inclusions is established, the question will be whether vesicle clustering is achieved in the absence of direct αS-αS interactions. An answer could be a 'double anchor' mechanism where one synuclein molecule can interact with two different vesicles, as was recently proposed (48). Several such connections via αS monomers could lead to larger vesicle clusters and, ultimately, to remodeling of the vesicles within the clusters (*e.g.* the tubulation seen by EM in Fig. 2). Some αS monomers stabilized at membranes may still be able to multimerize at least transiently, consistent with models of membrane-associated multimer formation that have been proposed by the Roy (6) and Südhof (28,49) labs.

With respect to αS pathology, we have so far not detected amyloid fibrils in our inclusions: EM images gave no indications of clear-cut, β-sheet-rich amyloid fibrils (Figs 2, 3 and 6D). However, early EM characterization of Lewy bodies showed the presence of many vesicles in the periphery of granular Lewy bodies (Fig. 4 in (50)) and Lewy body-related swellings (Figs 5 and 6 in (50)). Similar phenomena were described by other researchers (51,52) and numerous cored vesicles but few Lewy body filaments were found in an autopsy case of juvenile parkinsonism (53). Moreover, an association of synaptic proteins and LBs was described (54). These findings raise the possibility that the abnormal vesicle clusters we observe consistently in our tetramer-abrogating mutants are an early pathogenic step toward Lewy-type aggregates. Although membrane association has often been considered a physiological feature of αS biology (55,49) and has been associated with decreased amyloid fibril formation (56), it has also been reported to trigger pathological aggregation under certain conditions, apparently due to increased local αS concentration on membranes (35). In theory, the intimate association of αS with vesicles that we see in our acute inclusions could dissociate over longer times, leading to a core of abnormal αS fibrils and clusters of vesicles nearby in the periphery (Fig. 9C3 and 4). Moreover, our current data cannot

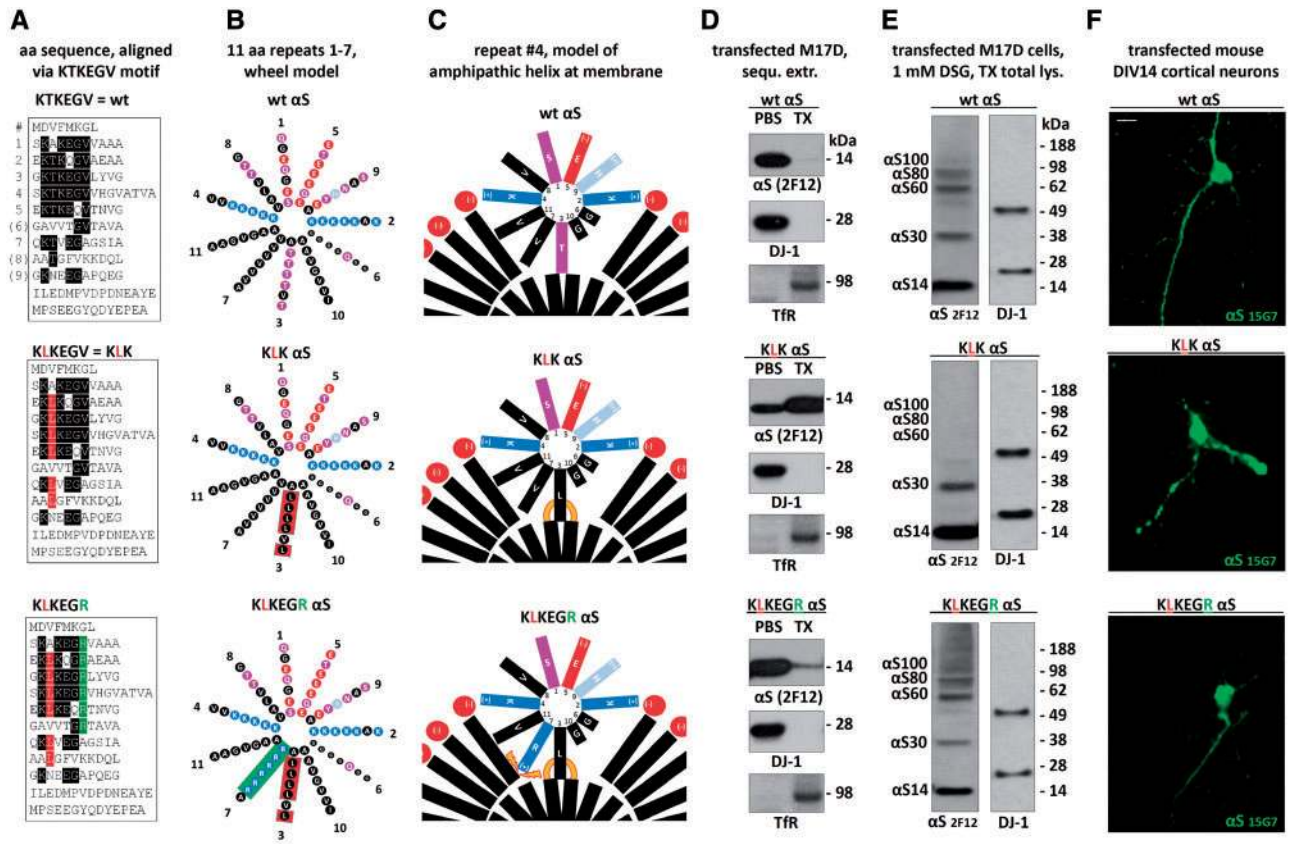

Figure 8. Rescuing the negative effects of αS KLK by introducing charged residues into the hydrophobic half of the αS amphipathic helix. (**A**) Schematics of αS wt, KLK and KLKEGR by aligning aa sequences via the repeat consensus sequence KTKEGV. (**B**) αS 11-residue repeats arranged in a helical wheel (a 3–11 helix: 3 turns over eleven residues). Blue indicates basic (light blue: histidine), red: acidic, purple: polar uncharged, and black: non-polar residues. (**C**) Schematic of αS repeat #4 embedded in the outer leaflet of a curved vesicle membrane (lipid head-groups in red, fatty acid 'tails' in black). Orange lines illustrate increased αS-membrane attraction, orange thunderbolts indicate increased αS-membrane repulsion. (**D**) WB for αS (mAb 2F12) in the PBS- or TX-100-soluble fractions of the indicated M17D transfectants. DJ-1 (cytosolic) and Transferrin receptor (membrane) served as controls; representative of three independent experiments. (**E**) wt, KLK and KLKEGR αS were transiently expressed in M17D cells for 48 h followed by *in vivo* cross-linking and WB; mAb 2F12 to αS; DJ-1 pAb as a control for equal loading and crosslinking. (**F**) Fluorescence microscopy of DIV14 mouse primary neurons transfected with the indicated untagged αS variants; human-specific αS mAb 15G7; scale bar, 20 μm; representative of three independent experiments.

rule out the possibility that the 3K and KLK mutations directly affect the tertiary structure of αS or that pathological oligomers and protofibrils may be present that are not readily resolved by immuno-EM. In this regard, certain engineered E→K αS mutations (E57K and E35K) expressed in a rat lentivirus model have been reported to inhibit fibril formation but stabilize pathologic oligomers (57), leading to dopaminergic loss in the substantia nigra. αS variants that formed mature amyloid fibrils very quickly were less toxic, and the authors speculated that abnormal αS oligomers might interact with and potentially disrupt membranes.

Lastly, very subtle changes in αS homeostasis (likely not yet accompanied by major misfolding events) can impair vesicle trafficking/function that then contributes to decreased cell viability, as observed in patient-derived neurons (58). It would be surprising if the multiple αS-positive vesicle clusters we describe in neural cells (Figs 1–5), in which vesicles derived from some but not all types of subcellular compartments aggregate and can no longer achieve their correct distributions, did not negatively affect the cells. It should be noted, however, that we cannot rule out that the excess binding of αS to vesicle membranes alone, even in the absence of aberrant clustering, is sufficient to impair vesicle trafficking, *e.g.* by stabilizing vesicle curvature and thereby preventing proper fusion with target membranes. In mature neurons *in vivo*, where much of αS is localized to synapses, an abnormal excess of monomers bound to synaptic vesicles (as seen in Fig. 6) could cause both subacute (Fig. 6A) and chronic (Fig. 6G and H) neurotoxicity. Based on the relatively subtle toxicity of prolonged overexpression in neurons (Fig. 6), we speculate that rodents expressing 3K or KLK αS could be viable but abnormal and serve as useful *in vivo* models to study the effects of chronic αS monomer-mediated vesicular clustering, as seen here in mammalian neural cells and previously in yeast (44,45). Such novel chronic models could also contribute to bridging two aspects of αS dyshomeostasis: impaired vesicle trafficking and Lewy-type αS aggregates.

Materials and Methods

All materials mentioned were purchased from Invitrogen unless stated otherwise.

Animal samples

Rodent samples were acquired under protocol number 05022 ('Mouse Models for Parkinson's Disease'), approved by the appropriate IACUC, the Harvard Medical Area Standing Committee

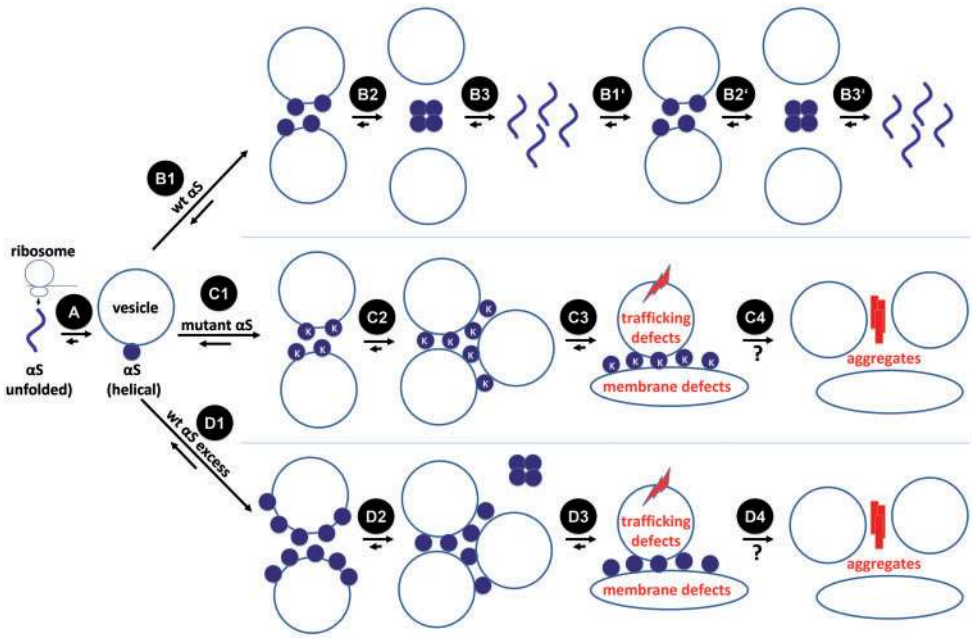

Figure 9. Model of αS homeostasis and dyshomeostasis in the context of transient vesicle binding. αS is translated on the ribosome as an unfolded monomer (**A**). Wt αS (at normal levels) binds to curved membranes and adopts helical folding (**B1**). αS-vesicle interactions could weaken when αS monomers multimerize (**B2**). Dynamic, metastable tetramers/multimers disassemble over time (**B3**), starting a new cycle (B1'-B3'). KTKEGV mutant monomers bind to membranes as well (**C1**), but their inability to multimerize may prolong their membrane dwell-time, thereby promoting vesicle-clustering (**C2**). The acute/subacute consequences may be defects in vesicle trafficking and membrane rearrangements such as tubulation (**C3**). A longer term consequence of higher local concentrations of αS monomers may be the gradual formation of β-sheet-rich αS aggregates (**C4**). Excess wt αS (**D1–D4**) as caused by *SNCA* gene duplication/triplication may result in similar defects, due to shifting of the physiological tetramer:monomer equilibrium toward excess free monomers (D2).

on Animals. Wt mice (C57BL/6; 12 wk old) were from Charles River, Wilmington, MA.

cDNA constructs

Plasmids pcDNA4/αS (21), pcDNA4/αS-3K (23), pcDNA4/αS-KLK (24), pcDNA4/αS-wt::YFP, pcDNA4/αS-3K::YFP (23), pcDNA4/αS-KLK::YFP (24), pcDNA4/αS-EIV::YFP (24) and pCAX/dsRed (23) have been described. αS-KLKEGR was synthesized as a GeneArt String DNA fragment (GeneArt/Life Technologies) and inserted into pcDNA4/TO/myc-His A (pcDNA4) with the In-Fusion HD Cloning Kit (Clontech). Plasmids mCherry-Rab5a-7 (Addgene plasmid # 55126), mCherry-Rab5a-7 (Addgene plasmid # 55127) mCherry-Rab11a-7 (Addgene plasmid # 55124), mCherry-SiT-N-15 (Addgene plasmid # 55133), mCherry-TFR-20 (Addgene plasmid # 55144), mCherry-ER-3 (Calreticulin; Addgene plasmid # 55041), mCherry-Endo-14 (RHOB; Addgene plasmid # 55040), mCherry-mito-7 (COX8A; Addgene plasmid # 55102), and mCherry-lysosomes-20 (LAMP1; Addgene plasmid # 55073) were kind gifts from Michael Davidson. pLVX-EF1α-IRES-mCherry vector was purchased from Clontech and viral constructs pLVX-IRES-mCherry/αS-wt, pLVX-IRES-mCherry/αS-3K and pLVX-IRES-mCherry/αS-KLK were generated by ligating SpeI/NotI digested PCR product into respective sites of pLVX-EF1α-IRES-mCherry. Previously described cDNA constructs (23,24) were used as templates for PCR amplification.

Production of lentiviral particles

Viral particles were produced by Lipofectamine 2000 based transfection of respective target constructs along with pMD2.G and psPAX2 (packaging plasmids: Addgene plasmid #12259 and #12260 respectively) into 293T cells. Culture supernatants containing viral particles were subsequently concentrated using Lenti-X^{TM} Concentrator (Clontech) as per manufacturer's protocol and on an average we obtained about 2.5×10^6 viral particles per μL.

Intact-cell crosslinking

Cells were collected by trituration, washed with PBS, and resuspended in PBS with Complete Protease Inhibitor, EDTA-free (Roche Applied Science). Crosslinkers DSG and DSP were prepared at 50 mM final concentration in DMSO immediately before use. Samples were incubated with crosslinker for 30 min at 37 °C with rotation. The reaction was quenched by adding Tris, pH 7.6, at 50 mM final concentration and incubated for 15 min at RT. After quenching, proteins were extracted (see below). DSG crosslinking occurred at 1 mM final concentration. 1.5 mM DSP-crosslinked samples underwent reductive cleavage by adding 5% (final concentration; w/v) βME to the sample buffer before boiling to maximize αS immunoblot detection by avoiding washing-off effects (22).

Protein extraction

To generate total protein extracts (cytosolic and membrane proteins), cells were lysed in 1% Triton-X 100 detergent (Sigma) by vortexing and incubation on ice for 20 min. Samples were then ultracentrifuged at 100,000*g* for 60 min at 4 °C to collect the supernatant. For sequential extraction, cells were lysed by sonication and centrifuged at 100,000*g* for 60 min, and the supernatant was collected (PBS cytosolic fraction). The pellet was solubilized in PBS/PI with 1% TX-100 and again centrifuged at 100,000*g* for 60 min. The resulting supernatant was collected (TX fraction: membrane proteins).

Immunoblotting

Protein concentrations were determined by BCA assay (Thermo Scientific). 20 μg of total protein were loaded per lane. Samples boiled in NuPAGE LDS sample buffer were electrophoresed on NuPAGE 4–12% Bis-Tris gels with NuPAGE MES-SDS running buffer and SeeBlue Plus2 marker. Gels were electroblotted onto Immobilon-Psq 0.2 μm PVDF membrane (Millipore) for 90 min at 400 mA at 4 °C in 25 mM Tris, 192 mM glycine, 20% methanol transfer buffer. Membranes were incubated in 0.4% paraformaldehyde, PBS for 30 min at RT, rinsed with PBS, stained with 0.1% Ponceau S in 5% acetic acid, rinsed with water and blocked in 0.2% IBlock solution (PBS containing 0.1% (v/v) Tween 20 (PBS-T) and 0.2% (w/v) IBlock) for either 30 min at RT or overnight at 4 °C. After blocking, membranes were incubated in primary antibody in 0.2% IBlock with 0.02% sodium azide for either 1 h at RT or overnight at 4 °C. Membranes were washed 3 × 10 min in PBS-T at RT and incubated 45 min at RT in horseradish peroxidase-conjugated secondary antibody (GE Healthcare) diluted 1:10,000 in 0.2% IBlock. Membranes were then washed 3 × 10 min in PBS-T and developed with SuperSignal West Dura (Thermo Scientific).

Cell culture and transfection

Cells were cultured at 37 °C in 5% CO_2. Human neuroblastoma cells (BE (2)-M17, called M17D; ATCC number CRL-2267) were cultured in Dulbecco's modified Eagle's medium (DMEM) supplemented with 10% FBS, 50 units per ml penicillin, 50 μg per ml streptomycin, and 2 mM L-glutamine. 293T cells used for lentiviral production (ATCC number CRL-3216) were cultured in DMEM supplemented with 10% FBS. Primary mouse neurons were cultured from CD-1 mice (Charles River, Wilmington, MA) as described (23). Cells were transfected using Lipofectamine 2000 (unsupplemented neurobasal medium instead of Opti-MEM for primary neurons) or transduced.

Stable cell pools and cell lines

Tet-on lines M17D-TR/αS-wt::YFP, M17D-TR/αS-3K::YFP, M17D-TR/αS-KLK::YFP were generated by Lipofectamine 2000 co-transfecting pcDNA6/TR and described plasmids pcDNA4/αS-wt::YFP, pcDNA4/αS-3K::YFP (23) and pcDNA4/αS-KLK::YFP (24), followed by Blasticidin (1 μg per mL) and Zeocin (200 ng per mL) selection. Expression was induced by adding 1 μg per ml (f.c.) dox to culture media. Lentivirally transduced pools were generated by infecting cells with titred virus at appropriate ratios. pcDNA4/αS-3K::YFP//RFP lines were generated by transducing pcDNA4/αS3K-wt::YFP with pLVX-IRES-mCherry (empty vector) viral particles.

Subcellular fractionation and gel filtration

1% TX-100 total protein lysates were loaded onto a 2.5–30% discontinuous Optiprep (Sigma) gradient, and run for 2.5 h at 200,000*g*. 1-ml fractions were collected, and 25-μl aliquots loaded onto an SDS gel. Size-exclusion chromatography (Superdex 200) was carried out as described (20).

Immunocytochemistry

Cells were grown on poly-D-lysine-coated surfaces, rinsed twice with HBSS with divalent cations, fixed 25 min at RT with 4% paraformaldehyde/PBS, then washed three times for 5 min with PBS. Cells were then blocked and permeabilized with 5% BSA/0.25% Triton X-100/PBS. Cells were incubated with primary antibody in block-permeabilizing buffer for 2 h at RT or overnight at 4 °C. After incubation with primary antibody, cells were washed 3 x 5 min with PBS, then incubated 1–2 h at RT with Alexa Fluor 488- and Alexa Fluor 568-coupled secondary antibodies diluted 1:2000 in 5% BSA/PBS (no Triton). Cells were washed 3 × 10 min at RT with PBS, then analyzed directly in the dish.

Antibodies

Antibodies used were monoclonals Syn-1 to αS (Clone 42, Becton-Dickinson; 1:2,000 in WB), 15G7 to αS (45) (hybridoma supernatants were 1:500 in WB and 1:50 in ICC), 2F12 (21) to αS (0.09 mg per ml in WB; commercially available as MABN1817, Millipore), 71.1 to GAPDH (Sigma; 1:5,000 in WB) as well as polyclonal antibodies C20 to αS (Santa Cruz; 1:1,000 for endogenous αS and 1:5,000–1:10,000 for transfectants in WB) pAb to DJ-1 (21), 4462 to Ran (Cell Signaling), ab8227 to β-actin (Abcam; 1:5,000 in WB), ab84036 to TfR (abcam; 1:1000 in ICC, 1:5000 in WB), FL-145 to TOM20 (Santa Cruz; 1:400 in ICC, 1:2000 in WB), ab22595 to Calnexin (abcam; 1:200 in ICC, 1:1000 in WB), PRB-114C to Giantin (Covance; 1:200 in ICC, 1:1000 in WB), ab24170 to Lamp1 (abcam; 1:200 in ICC, 1:1000 in WB), C8B1 to Rab5 (Cell Signaling; 1:200 in ICC, 1:1000 in WB), D95F2 to Rab7 (Cell Signaling; 1:200 in ICC, 1:1000 in WB), D4F5 to Rab11 (Cell Signaling; 1:200 in ICC, 1:1000 in WB) and ab32594 to synaptophysin (abcam; 1:200 in ICC).

Fluorescence microscopy

Fluorescence microscopy of cells in culture dishes was done on an AxioVert 200 microscope (AxioCam MRm camera; AxioVision Release 4.8.2; all by Zeiss, Jena, Germany). Images of YFP were collected using a GFP/FITC filter cube and are pseudo-colored green. Confocal images were obtained on a Zeiss LSM710 system.

Live-cell imaging

Cells were incubated (96 or 384 well plates) in the IncuCyte Zoom 2000 platform (Essen Biosciences) and images (red, green, bright field) were taken every 2 h. To measure inclusion formation in inducible M17D-TR/αS::YFP//RFP cells, we created the processing definition 'Inclusions'. Inclusions (green objects) were defined using the following parameters in the IncuCyte Zoom 2016A software: Top-Hat background subtraction, radius 10 μm, threshold (GCU) 5; Edge Split On, edge sensitivity 100; Cleanup, all parameters set to 0; Filters, Area (μm^2): min 0 and max 100, Eccentricity: min 0.1, Mean Intensity: min 9.5, Integrated Intensity: min 200.0. Cells were plated in 384-well plates at 10,000 cells per well and induced 24 h after plating. To measure the neurite length development of mouse neurons, we used the Neurotrack processing definition in the IncuCyte Zoom 2016A software and the following Cell-Body Clusters Parameters: Segmentation Mode: Brightness, Segmentation Adjustment: 0.4; Cleanup: Hole Fill (μm^2) 50.0 – Adjust Size (pixels) 0 – Min Cell Width (μm) 7.0; Cell Body Clusters Filters: Area (μm^2), min 100.0. The following Neurite Parameters were used: Filtering: Best; Neurite Sensitivity 0.5, Neurite Width (μm): 2. Primary mouse neurons were plated in 96-well plates at 50,000 cells per well and transduced on DIV2.

Electron microscopy

Cells were fixed in 2.5% glutaraldehyde, 1.25% paraformaldehyde, 0.03% picric acid in 0.1 M sodium cacodylate buffer (pH 7.4) for 1 h, washed 3x in 0.1M Cacodylate buffer, then postfixed in 1% Osmium tetroxide (OsO4)/1.5% Potassiumferrocyanide ($KFeCN_6$) for 30 min, washed in water 3x and incubated in 1% aqueous uranyl acetate for 30 min followed by two washes in water and subsequent dehydration in grades of alcohol (5 min each; 50%, 70%, 95%, 2x 100%). Cells were embedded in TAAB Epon (Marivac Canada Inc. St. Laurent, Canada) and polymerized at 60 °C for 48 h. Ultra-thin sections (about 80 nm) were cut on a Reichert Ultracut-S microtome and picked up on to copper grids. For immunogold labeling, the sections were etched using a saturated solution of sodium metaperiodate in water for 5 min at RT. Grids were then washed 3x in water and floated on 0.1% Triton-X-100 for 5 min at RT. Blocking was carried out using 1% BSA + 0.1% TX-100/PBS for an hour at RT. Grids were incubated with pAb C20 or anti-GFP antibody (1:50, Abcam 6556) in 1% BSA + 0.1% TX-100/PBS overnight at 4 °C. Grids were washed three times in PBS to remove unbound GFP antibody followed by incubation with 15nm Protein A-gold particles (Department of cell biology, University Medical Center Utrecht, the Netherlands) for an hour at RT. Grids were washed with PBS and water, stained with lead citrate and examined in a JEOL 1200EX Transmission electron microscope (JEOL USA Inc. Peabody, MA, USA) and images were recorded with an AMT 2k CCD camera.

Statistical analyses

Blinded analyses were performed by assigning random numbers to dishes or images by one investigator before representative images were taken or features were counted by another investigator. We performed one-way ANOVA including Tukey's (Figs 4C, 6E, F and H) or Dunnett's (Fig. 4B) multiple comparisons test as well as unpaired, two-tailed t-test (Fig. 6A) analyses using GraphPad Prism Version 7 following the program's guidelines. Normal distribution and similar variance were observed for all values. Graphs are means +/− S.D. Criteria for significance, routinely determined relative to wt αS: $^{*}P < 0.05$, $^{**}P < 0.01$, $^{***}P < 0.001$, $^{****}P < 0.0001$. Sufficient experiments and replicates were analyzed to achieve statistical significance and these judgements were based on earlier, similar work (23,24).

Acknowledgements

We thank N. Exner and C. Haass (Munich) for mAb 15G7, L. Doehr, C. Hoesch and G. Stirtz for contributing to data acquisition, and all members of the Selkoe, Khurana, LaVoie and Young-Pearse labs in the Ann Romney Center for Neurologic Diseases for many helpful discussions.

Conflict of Interest statement. DJS is a director and consultant to Prothena Biosciences. The other authors declare no conflict of interest.

Funding

NIH grant R01 NS083845 to DJS, a research grant from the Harvard Neurodiscovery Center to UD, a grant from the American Parkinson Disease Association to TB and a grant from the Parkinson's disease Foundation to OL. SF and SL were supported by the JPB Foundation. SL was an HHMI Investigator. The funders had no role in study design, data collection and analysis, decision to publish, or preparation of the manuscript.

References

1. Chandra, S., Fornai, F., Kwon, H.-B., Yazdani, U., Atasoy, D., Liu, X., Hammer, R.E., Battaglia, G., German, D.C., Castillo, P.E. *et al.* (2004) Double-knockout mice for alpha- and beta-synucleins: effect on synaptic functions. *Proc. Natl. Acad. Sci. U. S. A*, **101**, 14966–14971.
2. Abeliovich, A., Schmitz, Y., Fariñas, I., Choi-Lundberg, D., Ho, W.H., Castillo, P.E., Shinsky, N., Verdugo, J.M., Armanini, M., Ryan, A. *et al.* (2000) Mice lacking alpha-synuclein display functional deficits in the nigrostriatal dopamine system. *Neuron*, **25**, 239–252.
3. Nemani, V.M., Lu, W., Berge, V., Nakamura, K., Onoa, B., Lee, M.K., Chaudhry, F.A., Nicoll, R.A. and Edwards, R.H. (2010) Increased expression of alpha-synuclein reduces neurotransmitter release by inhibiting synaptic vesicle reclustering after endocytosis. *Neuron*, **65**, 66–79.
4. Scott, D. and Roy, S. (2012) α-Synuclein inhibits intersynaptic vesicle mobility and maintains recycling-pool homeostasis. *J. Neurosci.*, **32**, 10129–10135.
5. Bendor, J.T., Logan, T.P. and Edwards, R.H. (2013) The function of α-synuclein. *Neuron*, **79**, 1044–1066.
6. Wang, L., Das, U., Scott, D.A., Tang, Y., McLean, P.J. and Roy, S. (2014) α-synuclein multimers cluster synaptic vesicles and attenuate recycling. *Curr. Biol. CB.*, **24**, 2319–2326.
7. Vargas, K.J., Makani, S., Davis, T., Westphal, C.H., Castillo, P.E. and Chandra, S.S. (2014) Synucleins regulate the kinetics of synaptic vesicle endocytosis. *J. Neurosci.*, **34**, 9364–9376.
8. Schulz-Schaeffer, W.J. (2010) The synaptic pathology of alpha-synuclein aggregation in dementia with Lewy bodies, Parkinson's disease and Parkinson's disease dementia. *Acta Neuropathol. (Berl.)*, **120**, 131–143.
9. Schulz-Schaeffer, W.J. (2015) Is Cell Death Primary or Secondary in the Pathophysiology of Idiopathic Parkinson's Disease?. *Biomolecules*, **5**, 1467–1479.
10. Polymeropoulos, M.H., Lavedan, C., Leroy, E., Ide, S.E., Dehejia, A., Dutra, A., Pike, B., Root, H., Rubenstein, J., Boyer, R. *et al.* (1997) Mutation in the alpha-synuclein gene identified in families with Parkinson's disease. *Science*, **276**, 2045–2047.
11. Krüger, R., Kuhn, W., Müller, T., Woitalla, D., Graeber, M., Kösel, S., Przuntek, H., Epplen, J.T., Schöls, L. and Riess, O. (1998) Ala30Pro mutation in the gene encoding alpha-synuclein in Parkinson's disease. *Nat. Genet.*, **18**, 106–108.
12. Zarranz, J.J., Alegre, J., Gómez-Esteban, J.C., Lezcano, E., Ros, R., Ampuero, I., Vidal, L., Hoenicka, J., Rodriguez, O., Atarés, B. *et al.* (2004) The new mutation, E46K, of alpha-synuclein causes Parkinson and Lewy body dementia. *Ann. Neurol.*, **55**, 164–173.
13. Lesage, S., Anheim, M., Letournel, F., Bousset, L., Honoré, A., Rozas, N., Pieri, L., Madiona, K., Dürr, A., Melki, R. *et al.* (2013) G51D α-synuclein mutation causes a novel parkinsonian-pyramidal syndrome. *Ann. Neurol.*, **73**, 459–471.
14. Kiely, A.P., Asi, Y.T., Kara, E., Limousin, P., Ling, H., Lewis, P., Proukakis, C., Quinn, N., Lees, A.J., Hardy, J. *et al.* (2013) α-Synucleinopathy associated with G51D SNCA mutation: a link between Parkinson's disease and multiple system atrophy?. *Acta Neuropathol. (Berl.)*, **125**, 753–769.
15. Proukakis, C., Dudzik, C.G., Brier, T., MacKay, D.S., Cooper, J.M., Millhauser, G.L., Houlden, H. and Schapira, A.H. (2013)

A novel α-synuclein missense mutation in Parkinson disease. *Neurology*, **80**, 1062–1064.
16. Appel-Cresswell, S., Vilarino-Guell, C., Encarnacion, M., Sherman, H., Yu, I., Shah, B., Weir, D., Thompson, C., Szu-Tu, C., Trinh, J. *et al.* (2013) Alpha-synuclein p.H50Q, a novel pathogenic mutation for Parkinson's disease. *Mov. Disord.*, **28**, 811–813.
17. Singleton, A.B., Farrer, M., Johnson, J., Singleton, A., Hague, S., Kachergus, J., Hulihan, M., Peuralinna, T., Dutra, A., Nussbaum, R. *et al.* (2003) alpha-Synuclein locus triplication causes Parkinson's disease. *Science*, **302**, 841.
18. Chartier-Harlin, M.-C., Kachergus, J., Roumier, C., Mouroux, V., Douay, X., Lincoln, S., Levecque, C., Larvor, L., Andrieux, J., Hulihan, M. *et al.* (2004) Alpha-synuclein locus duplication as a cause of familial Parkinson's disease. *Lancet*, **364**, 1167–1169.
19. Fuchs, J., Tichopad, A., Golub, Y., Munz, M., Schweitzer, K.J., Wolf, B., Berg, D., Mueller, J.C. and Gasser, T. (2008) Genetic variability in the SNCA gene influences alpha-synuclein levels in the blood and brain. *FASEB J.*, **22**, 1327–1334.
20. Bartels, T., Choi, J.G. and Selkoe, D.J. (2011) α-Synuclein occurs physiologically as a helically folded tetramer that resists aggregation. *Nature*, **477**, 107–110.
21. Dettmer, U., Newman, A.J., Luth, E.S., Bartels, T. and Selkoe, D. (2013) *In vivo* cross-linking reveals principally oligomeric forms of α-synuclein and β-synuclein in neurons and non-neural cells. *J. Biol. Chem.*, **288**, 6371–6385.
22. Newman, A.J., Selkoe, D. and Dettmer, U. (2013) A new method for quantitative immunoblotting of endogenous α-synuclein. *PloS One*, **8**, e81314.
23. Dettmer, U., Newman, A.J., Soldner, F., Luth, E.S., Kim, N.C., von Saucken, V.E., Sanderson, J.B., Jaenisch, R., Bartels, T. and Selkoe, D. (2015) Parkinson-causing α-synuclein missense mutations shift native tetramers to monomers as a mechanism for disease initiation. *Nat. Commun.*, **6**, 7314.
24. Dettmer, U., Newman, A.J., von Saucken, V.E., Bartels, T. and Selkoe, D. (2015) KTKEGV repeat motifs are key mediators of normal α-synuclein tetramerization: Their mutation causes excess monomers and neurotoxicity. *Proc. Natl. Acad. Sci. U. S. A*, **112**, 9596–9601.
25. Wang, W., Perovic, I., Chittuluru, J., Kaganovich, A., Nguyen, L.T.T., Liao, J., Auclair, J.R., Johnson, D., Landeru, A., Simorellis, A.K. *et al.* (2011) A soluble α-synuclein construct forms a dynamic tetramer. *Proc. Natl. Acad. Sci. U. S. A*, **108**, 17797–17802.
26. Westphal, C.H. and Chandra, S.S. (2013) Monomeric synucleins generate membrane curvature. *J. Biol. Chem.*, **288**, 1829–1840.
27. Gould, N., Mor, D.E., Lightfoot, R., Malkus, K., Giasson, B. and Ischiropoulos, H. (2014) Evidence of native α-synuclein conformers in the human brain. *J. Biol. Chem.*, **289**, 7929–7934.
28. Burré, J., Sharma, M. and Südhof, T.C. (2014) α-Synuclein assembles into higher-order multimers upon membrane binding to promote SNARE complex formation. *Proc. Natl. Acad. Sci. U. S. A*, **111**, E4274–E4283.
29. Iljina, M., Tosatto, L., Choi, M.L., Sang, J.C., Ye, Y., Hughes, C.D., Bryant, C.E., Gandhi, S. and Klenerman, D. (2016) Arachidonic acid mediates the formation of abundant alpha-helical multimers of alpha-synuclein. *Sci. Rep.*, **6**, 33928.
30. Cole, N.B., Murphy, D.D., Grider, T., Rueter, S., Brasaemle, D. and Nussbaum, R.L. (2002) Lipid droplet binding and oligomerization properties of the Parkinson's disease protein alpha-synuclein. *J. Biol. Chem.*, **277**, 6344–6352.
31. Gurry, T., Ullman, O., Fisher, C.K., Perovic, I., Pochapsky, T. and Stultz, C.M. (2013) The dynamic structure of α-synuclein multimers. *J. Am. Chem. Soc.*, **135**, 3865–3872.
32. Fauvet, B., Mbefo, M.K., Fares, M.-B., Desobry, C., Michael, S., Ardah, M.T., Tsika, E., Coune, P., Prudent, M., Lion, N. *et al.* (2012) α-Synuclein in central nervous system and from erythrocytes, mammalian cells, and Escherichia coli exists predominantly as disordered monomer. *J. Biol. Chem.*, **287**, 15345–15364.
33. Theillet, F.-X., Binolfi, A., Bekei, B., Martorana, A., Rose, H.M., Stuiver, M., Verzini, S., Lorenz, D., van Rossum, M., Goldfarb, D. *et al.* (2016) Structural disorder of monomeric α-synuclein persists in mammalian cells. *Nature*, 10.1038/nature16531.
34. Burré, J., Vivona, S., Diao, J., Sharma, M., Brunger, A.T. and Südhof, T.C. (2013) Properties of native brain α-synuclein. *Nature*, **498**, E4-6-7.
35. Galvagnion, C., Buell, A.K., Meisl, G., Michaels, T.C.T., Vendruscolo, M., Knowles, T.P.J. and Dobson, C.M. (2015) Lipid vesicles trigger α-synuclein aggregation by stimulating primary nucleation. *Nat. Chem. Biol.*, **11**, 229–234.
36. Bussell, R., Ramlall, T.F. and Eliezer, D. (2005) Helix periodicity, topology, and dynamics of membrane-associated alpha-synuclein. *Protein Sci. Publ. Protein Soc.*, **14**, 862–872.
37. Jao, C.C., Hegde, B.G., Chen, J., Haworth, I.S. and Langen, R. (2008) Structure of membrane-bound alpha-synuclein from site-directed spin labeling and computational refinement. *Proc. Natl. Acad. Sci. U. S. A*, **105**, 19666–19671.
38. Wietek, J., Haralampiev, I., Amoussouvi, A., Herrmann, A. and Stöckl, M. (2013) Membrane bound α-synuclein is fully embedded in the lipid bilayer while segments with higher flexibility remain. *FEBS Lett.*, **587**, 2572–2577.
39. Zhu, M. and Fink, A.L. (2003) Lipid binding inhibits alpha-synuclein fibril formation. *J. Biol. Chem.*, **278**, 16873–16877.
40. George, J.M., Jin, H., Woods, W.S. and Clayton, D.F. (1995) Characterization of a novel protein regulated during the critical period for song learning in the zebra finch. *Neuron*, **15**, 361–372.
41. Irizarry, M.C., Kim, T.W., McNamara, M., Tanzi, R.E., George, J.M., Clayton, D.F. and Hyman, B.T. (1996) Characterization of the precursor protein of the non-A beta component of senile plaques (NACP) in the human central nervous system. *J. Neuropathol. Exp. Neurol.*, **55**, 889–895.
42. Perlmutter, J.D., Braun, A.R. and Sachs, J.N. (2009) Curvature dynamics of alpha-synuclein familial Parkinson disease mutants: molecular simulations of the micelle- and bilayer-bound forms. *J. Biol. Chem.*, **284**, 7177–7189.
43. Pranke, I.M., Morello, V., Bigay, J., Gibson, K., Verbavatz, J.-M., Antonny, B. and Jackson, C.L. (2011) αSynuclein and ALPS motifs are membrane curvature sensors whose contrasting chemistry mediates selective vesicle binding. *J. Cell Biol.*, **194**, 89–103.
44. Soper, J.H., Roy, S., Stieber, A., Lee, E., Wilson, R.B., Trojanowski, J.Q., Burd, C.G. and Lee, V.M.-Y. (2008) Alpha-synuclein-induced aggregation of cytoplasmic vesicles in Saccharomyces cerevisiae. *Mol. Biol. Cell*, **19**, 1093–1103.
45. Gitler, A.D., Bevis, B.J., Shorter, J., Strathearn, K.E., Hamamichi, S., Su, L.J., Caldwell, K.A., Caldwell, G.A., Rochet, J.-C., McCaffery, J.M. *et al.* (2008) The Parkinson's disease protein alpha-synuclein disrupts cellular Rab homeostasis. *Proc. Natl. Acad. Sci. U. S. A*, **105**, 145–150.
46. Kahle, P.J., Neumann, M., Ozmen, L., Muller, V., Jacobsen, H., Schindzielorz, A., Okochi, M., Leimer, U., van Der Putten, H., Probst, A. *et al.* (2000) Subcellular localization of wild-type

and Parkinson's disease-associated mutant alpha -synuclein in human and transgenic mouse brain. *J. Neurosci.*, **20**, 6365–6373.
47. Fortin, D.L., Troyer, M.D., Nakamura, K., Kubo, S., Anthony, M.D. and Edwards, R.H. (2004) Lipid rafts mediate the synaptic localization of alpha-synuclein. *J. Neurosci.*, **24**, 6715–6723.
48. Fusco, G., Pape, T., Stephens, A.D., Mahou, P., Costa, A.R., Kaminski, C.F., Kaminski Schierle, G.S., Vendruscolo, M., Veglia, G., Dobson, C.M. *et al.* (2016) Structural basis of synaptic vesicle assembly promoted by α-synuclein. *Nat. Commun.*, **7**, 12563.
49. Burré, J., Sharma, M. and Südhof, T.C. (2015) Definition of a Molecular Pathway Mediating α-Synuclein Neurotoxicity. *J. Neurosci.*, **35**, 5221–5232.
50. Forno, L.S. and Norville, R.L. (1976) Ultrastructure of Lewy bodies in the stellate ganglion. *Acta Neuropathol. (Berl.)*, **34**, 183–197.
51. Roy, S. and Wolman, L. (1969) Ultrastructural observations in Parkinsonism. *J. Pathol.*, **99**, 39–44.
52. Dickson, D.W., Crystal, H., Mattiace, L.A., Kress, Y., Schwagerl, A., Ksiezak-Reding, H., Davies, P. and Yen, S.H. (1989) Diffuse Lewy body disease: light and electron microscopic immunocytochemistry of senile plaques. *Acta Neuropathol. (Berl.)*, **78**, 572–584.
53. Hayashida, K., Oyanagi, S., Mizutani, Y. and Yokochi, M. (1993) An early cytoplasmic change before Lewy body maturation: an ultrastructural study of the substantia nigra from an autopsy case of juvenile parkinsonism. *Acta Neuropathol. (Berl.)*, **85**, 445–448.
54. Nishimura, M., Tomimoto, H., Suenaga, T., Nakamura, S., Namba, Y., Ikeda, K., Akiguchi, I. and Kimura, J. (1994) Synaptophysin and chromogranin A immunoreactivities of Lewy bodies in Parkinson's disease brains. *Brain Res.*, **634**, 339–344.
55. Davidson, W.S., Jonas, A., Clayton, D.F. and George, J.M. (1998) Stabilization of alpha-synuclein secondary structure upon binding to synthetic membranes. *J. Biol. Chem.*, **273**, 9443–9449.
56. Fonseca-Ornelas, L., Eisbach, S.E., Paulat, M., Giller, K., Fernández, C.O., Outeiro, T.F., Becker, S. and Zweckstetter, M. (2014) Small molecule-mediated stabilization of vesicle-associated helical α-synuclein inhibits pathogenic misfolding and aggregation. *Nat. Commun.*, **5**, 5857.
57. Winner, B., Jappelli, R., Maji, S.K., Desplats, P.A., Boyer, L., Aigner, S., Hetzer, C., Loher, T., Vilar, M., Campioni, S. *et al.* (2011) *In vivo* demonstration that alpha-synuclein oligomers are toxic. *Proc. Natl. Acad. Sci. U. S. A*, **108**, 4194–4199.
58. Chung, C.Y., Khurana, V., Auluck, P.K., Tardiff, D.F., Mazzulli, J.R., Soldner, F., Baru, V., Lou, Y., Freyzon, Y., Cho, S. *et al.* (2013) Identification and rescue of α-synuclein toxicity in Parkinson patient-derived neurons. *Science*, **342**, 983–987.